Astronomy & Astrophysics

Survey of intermediate/high mass star-forming regions at centimeter and millimeter wavelengths

Á. Sánchez-Monge[1], Aina Palau[1,2], R. Estalella[1], M. T. Beltrán[1], and J. M. Girart[3]

[1] Departament d'Astronomia i Meteorologia, Universitat de Barcelona, Martí i Franquès 1, 08028 Barcelona, Spain
e-mail: asanchez@am.ub.es
[2] Laboratorio de Astrofísica Espacial y Física Fundamental, INTA, Apartado 78, 28691 Villanueva de la Cañada, Madrid, Spain
[3] Institut de Ciències de l'Espai (CSIC-IEEC), Campus UAB – Facultat de Ciències, Torre C5 – parell 2, 08193 Bellaterra, Catalunya, Spain

ABSTRACT

Aims. The goal of this work is to characterize the millimeter and centimeter properties of intermediate/high mass young stellar objects (YSOs) to search for any evolutionary trends.
Methods. We carried out observations at 1.2 mm with the IRAM 30 m telescope, and at 3.6 and 1.3 cm with the VLA toward a sample of 11 luminous ($>10^3$ $L_\odot$) IRAS sources classified as high mass protostellar object candidates. The most promising regions additionally were observed at 7 mm with the VLA.
Results. The 1.2 mm emission, tracing the dust core in which the massive YSO is forming, shows a clear peak surrounded by some substructure in most cases, while in others it is very extended and weak. The masses from the 1.2 mm data range from 10 to 140 $M_\odot$. For all (but one) of the sources, we detected centimeter emission associated with the IRAS source, with spectral indices between 3.6 and 1.3 cm typical of optically thin emission, and deconvolved sizes from <0.01 to 0.3 pc, suggesting that the emission comes from compact or ultra-compact (UC) H II regions. The physical parameters of the UCH II regions indicate that the ionizing stars are early B-type. The 7 mm emission is partially resolved for the four regions observed at this wavelength, and we estimated the contribution of the dust emission to the 7 mm flux density, ranging from negligible to 45%. By combining our data with infrared surveys, we built the spectral energy distribution and fitted a modified blackbody law. We found dust temperatures between 25 and 35 K, dust emissivity indices between 1.5 and 2.2, and masses similar to the masses derived from the 1.2 mm continuum emission. In addition, we found a correlation between the degree of disruption of the natal cloud, estimated from the fraction of dust emission associated with the centimeter source relative to the total amount of dust in its surroundings, and the size of the centimeter source.
Conclusions. From the correlation found, we established an evolutionary sequence in which sources with compact millimeter emission clearly associated with compact centimeter emission are younger than sources with the millimeter emission dispersed and with the centimeter emission extended. Such a sequence is consistent with the evolutionary stage expected from maser/outflow/dense gas emission reported in the literature, and with the infrared excess of the 2MASS sources associated with the centimeter source.

Key words. stars: formation – ISM: dust, extinction – ISM: H II regions – radio continuum: ISM

1. Introduction

High mass stars ($M \gtrsim 10$ $M_\odot$) play a major role in the physical and chemical evolution of their host galaxies, through strong ultraviolet radiation and winds, and through supernova explosions. However, the formation scenario of these stars is not well understood, due to the large distances ($\gtrsim 1$ kpc) and heavy extinctions ($A_v \gtrsim 100$) of the regions in which they form. This, coupled with the fact that high mass stars seem to form in clustered mode (Testi et al. 1998, 2000; Hillenbrand 1995; Hillenbrand & Hartmann 1998), where a single massive dense core of gas forms a group of stars, makes it observationally more difficult to study these regions. A result recently found in massive star formation is that outflows, some of them collimated (e.g., Beuther et al. 2002; Gibb et al. 2003; Zhang et al. 2005), disk-like structures (e.g., Cesaroni et al. 1997, 1999; Patel et al. 2005), and infall motions (e.g., Beltrán et al. 2006a; Zapata et al. 2008) have been detected in massive protostars, suggesting that there is disk-mediated accretion in high mass stars, and that they may form as a scaled-up version of low mass stars. However, the different evolutionary stages describing how the massive protostar approaches the main sequence may differ from those for low mass stars, since massive stars evolve much faster to the main-sequence (e.g., Bernasconi & Maeder 1996), and, as a consequence, the massive protostar produces UV photons while still accreting matter. Thus, the centimeter emission, tracing the ionized gas, and the millimeter emission, usually tracing the dust, are crucial to understand the first stages in the formation of a massive star.

The work presented here is part of a large project aimed at studying in detail (with high sensitivity and high angular resolution) a sample of high mass star-forming regions ($L_{bol} \gtrsim 1000$ $L_\odot$) in different evolutionary stages, in order to characterize the millimeter and centimeter properties as the massive young stellar object (YSO) evolves. For this we selected, from the Molinari et al. (1996), Mueller et al. (2002), and Sridharan et al. (2002) samples, regions located at distances $\lesssim 3$ kpc, in order to be sensitive down to masses $\lesssim 1$ $M_\odot$ (from the millimeter emission), and to have a spatial resolution $\lesssim 5000$ AU. For each region, we searched the literature for centimeter and millimeter emission, and found 11 regions with no imaging at centimeter or millimeter observations. To complete the sample of

Table 1. List of regions observed in this work.

Region	L_{bol} ($L_\odot$)	Dist. (kpc)	Instrument[a]	Ref.
IRAS 00117+6412	1300	1.8	V + I	1
IRAS 04579+4703	4000	2.5	V + I	1
IRAS 18123−1203	7900	3.1	V + I	1
IRAS 18171−1548[b]	7900	2.6	V + I	1
IRAS 18212−1320	1600	2.2	I	1
IRAS 19045+0813	1600	1.6	V + I	1
IRAS 20293+4007	7900	3.4	V + I	1
IRAS 22187+5559	7900	2.9	V + I	1
IRAS 22198+6336	1300	1.3	V	1
NGC 7538-IRS9[c]	40 000	2.8	V	2
IRAS 23448+6010	2500	2.0	V + I	1

[a] V: VLA, I: IRAM 30 m.
[b] This source appears as IRAS 18172−1548 in Molinari et al. (1996).
[c] Identified with IRAS 23118+6110.
References: (1) Molinari et al. (1996), (2) Mueller et al. (2002).

nearby and luminous massive star-forming regions observed at millimeter and centimeter wavelengths, we carried out VLA and IRAM 30 m observations toward these 11 regions. Nine regions were observed in the millimeter range, and 10 in the centimeter range (8 coinciding with the regions observed at millimeter wavelengths, see Table 1).

In Sect. 2, we summarize the observations, in Sect. 3 we give the general results, in Sect. 4 we discuss the nature of the centimeter emission, comment on the results for each individual source, and discuss global properties that possibly indicate different evolutionary stages of the massive YSOs. In Sect. 5 we summarize our main conclusions.

2. Observations

The MPIfR 117-element bolometer array MAMBO-2 at the IRAM 30 m telescope[1] was used to map the 1.2 mm dust continuum emission toward the 9 selected high mass protostar candidates (see Table 1). The observations were carried out on 2004 January 23 to 25. The main beam of the IRAM 30 m at 1.2 mm has a HPBW size of 11″. We used the on-the-fly mapping mode, in which the telescope scans in azimuth along each row in such a way that all pixels see the source once. The sampled area was typically 320″ × 80″, and the scanning speed was 6″ s^{-1}. Each scan was separated by 8″ in elevation. The secondary mirror was wobbling at a rate of 2 Hz in azimuth with a wobbler throw of 70″. The average zenith opacity at 225 GHz was 0.3−0.4. The overall uncertainty in calibration is estimated to be 20%. Data reduction was performed with the MOPSIC software package (distributed by R. Zylka).

The centimeter observations were carried out on 2004 July 10 and 13 using the Very Large Array (VLA) of the NRAO[2] in the D configuration. The regions observed at 3.6 cm, the phase calibrators used and their bootstrapped fluxes, as well as the parameters of the synthesized beam, the robust parameter of Briggs (1995), and the rms noise of the maps are given in Table 2, and the same information for 1.3 cm is given in Table 3. The positions of the phase centers correspond

to the coordinates given in Molinari et al. (1996) or Mueller et al. (2002). In all cases, except for IRAS 19045+0813 and NGC 7538-IRS9, they correspond to the catalog positions of the IRAS sources. The integration time for each source was about 5 min at 3.6 cm and 11 min at 1.3 cm. Absolute flux calibration was achieved by observing 3C 48, with an adopted flux density of 3.15 Jy and 1.12 Jy at 3.6 and 1.3 cm, and 3C 286, with 5.21 Jy and 2.52 Jy at 3.6 and 1.3 cm respectively. Images were constructed using a variety of weighting schemes by varying the Briggs robust parameter from +1 to +5 (roughly equivalent to the natural weight) for most of the regions (see Table 2 and 3). In order to increase the SNR of the faint sources at 1.3 cm, we tapered the uv-data at 50 kλ, except for IRAS 22187+5559, for which we tapered the uv-data at 25 kλ, in order to recover the extended emission.

The 7 mm observations carried out toward four regions (see Table 4) were made with the VLA in the D configuration during the first months of 2007, with 8 EVLA antennas in the array. In order to minimize the effects of atmospheric phase fluctuations, we used the technique of *fast switching* (Carilli & Holdaway 1997) between the source and the phase calibrator over a cycle of 120 s, with 80 s spent on the target and 40 s on the calibrator. The integration time for each source was about 50 min, except for IRAS 04579+4703 with an on-source time of about 100 min. The images were constructed using natural weighting and tapering the uv-data at 60 kλ, except for IRAS 22198+6336, to increase the SNR.

For simplicity, we will refer to each IRAS source by an "I" followed by the RA identification of the catalog name.

3. Results

3.1. Results at 1.2 mm

In Table 5 we summarize the main results of the IRAM 30 m observations, in particular the peak intensity, flux density, and mass of gas and dust for each region. We estimated the mass of the dust component at 1.2 mm assuming a dust temperature of 30 K, and a dust mass opacity coefficient of 0.9 cm^2 g^{-1} at 1.2 mm (Ossenkopf & Henning 1994). In the bottom panel of Figs. 1 to 10 we show in grey scale and black contours the 1.2 mm continuum emission.

None of the regions observed with the IRAM 30 m shows a point-like morphology. On the contrary, four regions (I18123, I18171, I20293, and I23448) have very extended emission, with no clear peak. The other regions have a clear emission peak and show some substructure. For I18212 no millimeter source was detected (<620 mJy). Thus, this source was not observed with the VLA.

3.2. Results at 3.6 cm, 1.3 cm, and 7 mm

In Tables 6−8 we list all the sources detected in each region above the 5σ level at 3.6 cm, 1.3 cm, and 7 mm respectively. The three tables give, for each centimeter source identified in each region (labeled in increasing RA), the coordinates, peak intensity, flux density, and deconvolved size and position angle obtained by fitting a Gaussian with the task JMFIT in AIPS. In all three tables, we classify a VLA source as "central" if it is located within the central 50″ of diameter around the IRAS source, corresponding to 0.5 pc at an average distance of 2 kpc, the expected size of the cluster forming around a high mass source (Hillenbrand & Hartmann 1998; Testi et al. 1999). For sources

Table 2. Parameters of the observations at 3.6 cm with the VLA.

Region	Phase center[a]		Phase Calibrator	Bootstrapped flux (Jy)	Beam (arcsec)	PA (°)	Robust	rms (μJy beam^{-1})
	α(J2000.0)	δ(J2000.0)						
IRAS 00117+6412	00 14 27.73	+64 28 46.2	0102+584	1.885 ± 0.003	14.9 × 8.5	76	+1	38
IRAS 04579+4703	05 01 39.73	+47 07 23.1	0423+418	1.986 ± 0.004	10.7 × 9.4	48	+5	22
IRAS 18123−1203	18 15 07.33	−12 02 42.0	1822−096	1.364 ± 0.002	12.3 × 8.1	5	+1	43
IRAS 18171−1548	18 20 04.62	−15 46 46.6	1822−096	1.364 ± 0.002	13.0 × 8.1	2	+1	185
IRAS 19045+0813	19 06 59.77	+08 18 42.8	1922+155	0.666 ± 0.002	8.9 × 7.8	43	−3	54
IRAS 20293+4007	20 31 07.92	+40 17 22.8	2025+337	1.826 ± 0.003	7.5 × 6.5	−37	−5	58
IRAS 22187+5559	22 20 34.89	+56 14 39.5	2148+611	0.971 ± 0.003	7.8 × 6.6	−1	−5	155
IRAS 22198+6336	22 21 27.62	+63 51 42.2	2148+611	0.971 ± 0.003	10.4 × 8.8	7	+5	27
NGC 7538-IRS9	23 14 01.68	+61 27 19.9	0014+612	1.343 ± 0.004	10.2 × 9.3	−14	+5	700[b]
IRAS 23448+6010	23 47 20.07	+60 27 21.1	0102+584	1.753 ± 0.003	10.0 × 8.7	4	+5	30

[a] Units of right ascension are hours, minutes, and seconds, and units of declination are degrees, arcminutes, and arcseconds.
[b] rms limited by dynamic range.

Table 3. Parameters of the observations at 1.3 cm with the VLA.

Region	Phase center[a]		Phase Calibrator	Bootstrapped flux (Jy)	Beam (arcsec)	PA (°)	Robust	rms (μJy beam^{-1})
	α(J2000.0)	δ(J2000.0)						
IRAS 00117+6412	00 14 27.73	+64 28 46.2	0102+584	2.256 ± 0.015	5.9 × 4.5	−21	+5	67
IRAS 04579+4703	05 01 39.73	+47 07 23.1	0423+418	1.617 ± 0.017	5.4 × 4.4	45	+5	85
IRAS 18123−1203	18 15 07.33	−12 02 42.0	1832−105	0.913 ± 0.015	6.9 × 4.6	−20	+5	63
IRAS 18171−1548	18 20 04.62	−15 46 46.6	1832−105	0.913 ± 0.015	8.3 × 5.0	−34	+5	112
IRAS 19045+0813	19 06 59.77	+08 18 42.8	1922+155	0.504 ± 0.002	6.0 × 4.2	41	+4	65
IRAS 20293+4007	20 31 07.92	+40 17 22.8	2025+337	1.946 ± 0.013	5.1 × 4.3	41	+5	80
IRAS 22187+5559	22 20 34.89	+56 14 39.5	2137+510	0.626 ± 0.008	7.9 × 6.5	50	+5	60
IRAS 22198+6336	22 21 27.62	+63 51 42.2	2230+697	0.601 ± 0.005	3.6 × 2.9	−5	+1	63
NGC 7538-IRS9	23 14 01.68	+61 27 19.9	2230+697	0.601 ± 0.005	3.7 × 3.1	14	−5	204
IRAS 23448+010	23 47 20.07	+60 27 21.1	0102+584	2.256 ± 0.015	5.3 × 4.3	40	+5	76

[a] Units of right ascension are hours, minutes, and seconds, and units of declination are degrees, arcminutes, and arcseconds.

Table 4. Parameters of the observations at 7 mm with the VLA.

Region	Phase center[a]		Phase Calibrator	Bootstrapped flux (Jy)	Beam (arcsec)	PA (°)	Robust	rms (μJy beam^{-1})
	α(J2000.0)	δ(J2000.0)						
IRAS 04579+4703	05 01 39.73	+47 07 23.1	0502+416	0.424 ± 0.012	3.7 × 3.2	40	+5	94
IRAS 19045+0813	19 06 59.77	+08 18 42.8	1856+061	0.249 ± 0.006	3.9 × 3.3	44	+5	100
IRAS 22187+5559	22 20 34.89	+56 14 39.5	2250+558	0.300 ± 0.019	3.6 × 3.1	49	+5	178
IRAS 22198+6336	22 21 27.62	+63 51 42.2	2148+611	0.530 ± 0.032	2.2 × 1.3	−43	+0	226

[a] Units of right ascension are hours, minutes, and seconds, and units of declination are degrees, arcminutes, and arcseconds.

with extended emission, we estimated the intensity peak and flux density using the TVSTAT task in AIPS.

In the case of NGC 7538-IRS9 at 3.6 cm, the rms was limited by the dynamic range of the strong source VLA 1 (NGC 7538-IRS1) and the extended emission toward the north of VLA 1 (which corresponds to an H II region detected at 21 cm, see Fig. 9). We performed self-calibration in phase by using the strong source VLA 1. Subsequently, we substracted the clean components of VLA 1 using the task UVSUB in AIPS and used different uv-ranges in order to better clean the extended emission and reduce the rms noise. Although the rms noise was lowered from 1.28 to 0.7 mJy beam^{-1}, this was not low enough to detect VLA 2 and VLA 3, for which Sandell et al. (2005) report a flux density of 0.76 ± 0.15 mJy.

We estimated the spectral index α ($S_\nu \propto \nu^\alpha$) of the central sources, listed in Table 9, using the flux densities at 3.6 and 1.3 cm. In order to properly compare the flux at both wavelengths, we made 3.6 and 1.3 cm images using the same uv-range (4−25 kλ) at both wavelengths. For the sources not detected at both wavelengths in the 4−25 kλ maps, we used the flux densities obtained with no restrictions in the uv-range, listed

in Tables 6 or 7. The upper limit for non-detections was set to 4 times the rms noise level of the map, or slightly higher for extended sources. For details of the calculation of the spectral indices see the footnotes to Table 9.

Additionally, we searched the NRAO VLA Sky Survey (NVSS, Condon et al. 1998) for emission at 21 cm, and estimated the spectral index between 21 and 3.6 cm. We made new images at 3.6 cm with a uv-range of projected baselines of 1−5 kλ, which corresponds to the uv-range of the NVSS images. In the case of non-detection we followed the same procedure described above.

For the four regions additionally observed at 7 mm (I04579, I19045, I22187, and I22198), we detected emission in all the cases (see Table 8), with I19045 being the faintest source. For all the sources, the 7 mm emission was partially resolved. We estimated the contribution of ionized gas to the 7 mm emission by using the spectral index from 3.6 to 1.3 cm (Table 9) and extrapolating the flux density at 1.3 cm (Table 7) to 7 mm. From the estimated free-free flux density at 7 mm and the total observed flux density (from Table 8), we estimated the contribution from dust at 7 mm, which was ~38% for the case of I04579, ~44% for

Table 5. Parameters of the 1.2 mm sources observed with IRAM 30 m.

Region	rms (mJy beam^{-1})	I_ν^{peak} (mJy beam^{-1})	S_ν^a (mJy)	Mass^b ($M_\odot$)
IRAS 00117+6412	8	108	1200	36
IRAS 04579+4703	7	92	390	23
IRAS 18123−1203	15^c	68	440	41
IRAS 18171−1548	16^c	74	2200	142
IRAS 18212−1320	14^c	<56	<620	…
IRAS 19045+0813	9	100	390	10
IRAS 20293+4007	9	55	570	64
IRAS 22187+5559				
VLA 3^d	7	46	180	14
VLA 5^d	7	86	390	32
IRAS 23448+6010	11	63	1600	63

^{a} Flux density inside an aperture of 80″ of diameter, except for IRAS 22187+5559, where the aperture was 50″ for the source associated with VLA 5 and 30″ for the source associated with VLA 3.
^{b} Mass of gas and dust derived assuming T_d = 30 K, and a dust mass opacity coefficient of 0.9 cm^2 g^{-1} at 1.2 mm (Ossenkopf & Henning 1994).
^{c} High rms noise due to the low elevation of the sources at the time of the observations.
^{d} See Sect. 4.2.7.

I22198, and negligible for I19045 and I22187 (Table 11). We additionally estimated the mass of the dust component at 7 mm assuming a dust temperature in the 50−100 K range (Gómez et al. 2003), a dust emissivity index of 2 and a dust mass opacity coefficient of 0.9 cm^2 g^{-1} at 1.2 mm (Ossenkopf & Henning 1994). Note that we assumed a higher temperature for the dust emission at 7 mm than for the IRAM 30 m emission at 1.2 mm, because the IRAM 30 m emission must come mainly from the (large-scale) envelope of the massive object, while the 7 mm emission traces the compact dust component possibly related to a disk, which must be hotter than the envelope. The resulting masses for the 7 mm dust components are listed in Table 11.

Figures 1 to 10 show the maps for each region. For most of the regions there are two main panels showing the K-band of the Two Micron All Sky Survey (2MASS), and the IRAM 30 m 1.2 mm continuum emission, together with the VLA 3.6 and 1.3 cm continuum emission, and 7 mm continuum emission when available. For regions with sources beyond the central ∼50″ around the IRAS source (Figs. 3, 5, and 6), there is an extra top panel showing the area covered by the primary beam at 3.6 cm (∼5′).

3.3. Infrared photometry from 2MASS and IRAC-Spitzer

For each region, we downloaded the sources of the 2MASS catalog within the VLA primary beam at 3.6 cm, and we estimated for each 2MASS source the infrared excess from the ($J − H$) vs. ($H − K$) diagram, measured as the difference between the ($H − K$) color and the ($H − K$) color corresponding to a reddened main-sequence star (following the reddening law of Rieke & Lebofsky 1985). We assigned a color and a different star symbol to each infrared excess interval: three-point blue stars for infrared excesses <−0.4; four-point green stars for the interval (−0.4−0), corresponding to main-sequence stars, giants, and Class III and II sources with small infrared excess; five-point yellow stars for (0−0.4), corresponding to Class II sources; six-point orange stars

for (0.4−1), corresponding to Class I sources, and ten-point red stars for infrared excesses >1 (Matsuyanagi et al. 2006). The 2MASS sources are marked as stars with the corresponding color in Figs. 1 to 10. In our sample, I04579 and NGC 7538-IRS9 are the two regions where the 2MASS source associated with the IRAS source shows the largest infrared excess. Large infrared excesses are interpreted as reflecting an early evolutionary stage not only for low mass YSOs (e.g., Strom et al. 1993; Kenyon & Hartmann 1995), but also for intermediate/high mass YSOs (e.g., Massi et al. 1999; Nürnberger 2003).

In addition, I18171 and I19045 were observed with IRAC-*Spitzer*, whose images are shown in Kumar & Grave (2007). For these two regions, we studied the IRAC sources within the central 120″ around the UCH II region, and plotted the sources in K−[3.6] vs. [3.6]−[4.5] and [3.6]−[4.5] vs. [4.5]−[5.8] diagrams, allowing us to distinguish between Class II/III and Class 0/I sources (Allen et al. 2004; Hartmann et al. 2005; Getman et al. 2007). For simplicity, in Figs. 4 to 5 we plotted only the IRAC sources classified as Class 0/I sources and with no 2MASS counterpart. We contrasted the classification of YSOs from IRAC colors with the classification from JHK infrared excess (described above) and found that in general IRAC and 2MASS colors yield a similar classification. Thus, for the regions not observed with IRAC we consider the classification of YSOs from JHK infrared excess as a first valid approach to the evolutionary stage of each source.

3.4. Spectral energy distributions

We searched the literature for data from 2MASS, IRAC-*Spitzer*, MSX, and SCUBA (Di Francesco et al. 2008) for each region. We found an infrared counterpart of the IRAS source for all the cases except for I22198. With these data, and the data presented in this work, we built the SED for each IRAS source, and fitted a modified blackbody law for the far-infrared to millimeter data, taking into account the contribution of a free-free optically thin law for the centimeter data. Note that we did not attempt to fit the near/mid-infrared emission coming from components with higher temperatures. We adopted a dust mass opacity coefficient at 1.2 mm of 0.9 cm^2 g^{-1} (Ossenkopf & Henning 1994), a gas-to-dust mass ratio of 100, and assumed that the opacity follows a power law. The modified blackbody law allowed us to estimate a range of masses, dust temperatures, and dust emissivity indices associated with the envelope of each intermediate/high mass YSO (see Table 11 and Fig. 11). The median values were ∼25 $M_\odot$, ∼29 K, and 1.9, respectively. Dust temperatures and dust emissivity indices obtained in this work are similar to those obtained by Mookerjea et al. (2007) toward a sample of high mass protostellar objects located in the outer Galaxy. For I20293 and I23448 we did not build the SED because the millimeter peak and the UCH II region (associated with the IRAS source for I23448) are separated by ∼25″ and 40″, respectively, and could be tracing different objects.

Regarding the contribution of the free-free emission, we adopted the spectral index listed in Table 9 (for NGC 7538-IRS9 the spectral index used in the fit corresponds to −0.1). For I22198 we downloaded 21 cm and 6 cm VLA continuum data from the archive (project AO145) and reduced it. At the position of VLA 2 we found a compact source at 21 cm and 6 cm, with a flux density of 0.23 ± 0.05 mJy and 0.38 ± 0.03 mJy, respectively. These values are in agreement with those obtained by us at 3.6 cm, 1.3 cm and 7 mm (see the SED in Fig. 11).

Table 6. Parameters of the sources detected at 3.6 cm.

Region	VLA source	Central source[a]	α(J2000.0) (h m s)	δ(J2000.0) (° ′ ″)	$I_\nu^{\text{peak}\ b}$ (mJy beam^{-1})	S_ν [b] (mJy)	Deconv. Size (″)	PA (°)
IRAS 00117+6412	2–3[c]	Y	00 14 28.12	+64 28 46.2	1.23 ± 0.04	1.61 ± 0.08	8.8 × 4.3	73
IRAS 04579+4703	1	Y	05 01 39.92	+47 07 21.1	0.15 ± 0.03	0.15 ± 0.04	3.3 × 0.0	30
IRAS 18123−1203	1	N	18 15 01.36	−12 01 43.2	0.27 ± 0.05	0.88 ± 0.23	19.2 × 11.1	163
	2	Y	18 15 07.55	−12 01 43.3	0.22 ± 0.04	0.45 ± 0.12	12.2 × 8.1	19
	3	N	18 15 08.01	−12 05 10.0	2.25 ± 0.09[d]	2.62 ± 0.17[d]	5.4 × 2.9	2
	4	Y	18 15 08.05	−12 01 58.0	0.23 ± 0.04	0.53 ± 0.14	12.4 × 9.5	107
	5	Y	18 15 08.12	−12 01 38.0	0.30 ± 0.04	0.58 ± 0.12	10.4 × 8.2	81
	6	Y	18 15 08.75	−12 01 58.0	0.23 ± 0.04	0.43 ± 0.12	10.9 × 6.1	104
	7	N	18 15 14.42	−11 59 32.0	0.79 ± 0.16[d]	1.85 ± 0.55[d]	15.2 × 8.0	52
IRAS 18171−1548	1	Y	18 20 06.40	−15 46 44.1	1.57 ± 0.21	3.42 ± 0.63	12.2 × 9.9	18
IRAS 19045+0813	1	N	19 06 50.61	+08 19 20.6	0.50 ± 0.05[d]	0.54 ± 0.09[d]	4.1 × 0.0	64
	2	Y	19 06 58.64	+08 18 58.3	0.23 ± 0.05	0.38 ± 0.11	16.2 × 0.0	21
	3	Y	19 06 59.34	+08 18 56.7	0.41 ± 0.04	0.97 ± 0.14	12.3 × 7.2	91
	4	Y	19 06 59.63	+08 19 08.9	0.54 ± 0.04	1.41 ± 0.15	15.5 × 6.4	48
	5	Y	19 06 59.77	+08 19 19.1	0.30 ± 0.04	0.52 ± 0.11	10.3 × 2.4	156
	6	Y	19 07 00.12	+08 19 09.9	0.50 ± 0.04	1.32 ± 0.15	13.2 × 7.7	130
	2–6[c]	Y	…	…	0.56 ± 0.13	3.14 ± 0.19	…	…
	7	Y	19 07 00.45	+08 18 44.5	0.59 ± 0.05	0.60 ± 0.08	3.4 × 0.0	152
IRAS 20293+4007	1	Y	20 31 07.17	+40 17 20.9	0.87 ± 0.06	2.84 ± 0.24	12.4 × 8.7	22
	2	Y	20 31 07.19	+40 17 27.1	0.72 ± 0.06	2.08 ± 0.22	10.6 × 8.7	179
	1–2[c]	Y	…	…	0.90 ± 0.22	3.79 ± 0.31	…	…
	3	N	20 31 19.11	+40 18 09.7	1.39 ± 0.10[d]	1.63 ± 0.20[d]	4.4 × 0.0	72
IRAS 22187+5559	1	Y	22 20 32.01	+56 14 53.5	1.59 ± 0.24	1.71 ± 0.24	…	…
	2	Y	22 20 33.45	+56 15 01.5	2.24 ± 0.37	3.31 ± 0.37	…	…
	3	Y	22 20 33.67	+56 14 26.4	3.25 ± 0.10	32.58 ± 1.10	39.0 × 10.7	128
	4	Y	22 20 34.51	+56 14 57.6	3.21 ± 0.10	20.10 ± 0.72	19.3 × 13.9	155
	5	Y	22 20 35.58	+56 14 45.3	5.59 ± 0.10	38.18 ± 0.78	21.3 × 14.0	170
	1–5[c]	Y	…	…	5.96 ± 1.06	109 ± 2	…	…
IRAS 22198+6336	1	N	22 21 24.48	+63 52 20.2	0.30 ± 0.02	0.30 ± 0.03	2.2 × 0.0	26
	2	Y	22 21 26.68	+63 51 38.2	0.59 ± 0.02	0.57 ± 0.03	1.5 × 0.0	171
NGC 7538-IRS9 [e]	1	N	23 13 45.47	+61 28 19.7	800 ± 10[d]	1360 ± 30[d]	10.2 × 6.0	4
IRAS 23448+6010	1	Y	23 47 16.29	+60 27 13.6	0.39 ± 0.03	0.56 ± 0.06	13.3 × 0.0	176
	2	Y	23 47 20.08	+60 27 22.8	0.40 ± 0.03	1.91 ± 0.14	23.7 × 13.4	151
	4	Y	23 47 21.97	+60 27 48.3	0.21 ± 0.03	0.53 ± 0.09	14.8 × 8.6	78
	5	Y	23 47 22.47	+60 27 12.7	0.29 ± 0.03	0.90 ± 0.10	15.0 × 11.7	112
	6	Y	23 47 23.21	+60 27 33.8	0.26 ± 0.03	0.60 ± 0.08	13.4 × 8.6	7
	2–6[c]	Y	…	…	0.40 ± 0.10	3.19 ± 0.13	…	…

[a] Y = source within the central 50″ around the IRAS source; N = source out of the central 50″ around the IRAS source.

[b] Intensity and flux density corrected for primary beam response.

[c] Emission from the sources included in the range.

[d] Primary beam correction factor greater than 1.5.

[e] Extended emission is found toward the north of VLA 1, with an intensity peak of ~50 mJy beam^{-1} and a flux density of ~1.8 Jy. The coordinates of the intensity peak are α(J2000.0) = 23^{h}13^{m}32^{s}63, and δ(J2000.0) = +61°29′53″7 (see Fig. 9).

4. Discussion

4.1. On the nature of the cm emission associated with IRAS sources

Most of the sources classified as central sources in Tables 6 and 7 have a flat or positive spectral index (see Table 9). All of them (with the exception of I18123) are nearly coincident with the corresponding IRAS source, which in all cases has a bolometric luminosity $\gtrsim 10^3\ L_\odot$, suggesting that the centimeter sources associated with the IRAS source are tracing UCH II regions. However, the centimeter emission from the sources associated with molecular outflows, I22198 and NGC 7538-IRS9, could also arise in gas ionized by shocks in the outflow. The centimeter continuum luminosity, $S_\nu d^2$, from shock-ionized gas is proportional to the outflow momentum rate, $\dot P$, with a constant

of proportionality including an efficiency factor, η, defined as the fraction of the stellar wind that is shocked (Curiel et al. 1987). For low mass YSOs, Anglada (1995) found that the centimeter emission can be produced by shock-ionized gas with efficiencies of 10%. In our case, the efficiencies needed to account for the observed centimeter emission should be much higher than those observed for low mass YSOs, ~90% for I22198 and ~50% for NGC 7538-IRS9, it being reasonable to assume that, at least for these two sources, the contribution of shock-ionized gas is only a small fraction of the observed continuum centimeter emission. Since these two sources seem to be among the youngest in our sample (see Sect. 4.3), the contribution of shock-ionized gas in the other sources is expected also to be a small fraction of the observed centimeter emission. Thus, the centimeter sources associated with the IRAS source are most likely tracing compact

Table 7. Parameters of the sources detected at 1.3 cm.

Region	VLA source	Central source[a]	α(J2000.0) (h m s)	δ(J2000.0) (° ′ ″)	$I_\nu^{\text{peak}\ b}$ (mJy beam^{-1})	$S_\nu^{\ b}$ (mJy)	Deconv. Size (″)	PA (°)
IRAS 00117+6412	1	N	00 14 22.26	+64 28 28.7	0.47 ± 0.08	0.39 ± 0.14	unresolved	–
	2	Y	00 14 28.32	+64 28 41.2	0.47 ± 0.06	0.70 ± 0.15	6.0 × 0.0	57
	3	Y	00 14 28.43	+64 28 47.7	0.57 ± 0.06	1.24 ± 0.19	5.9 × 5.2	119
	2–3[c]	Y	…	…	0.59 ± 0.15	1.72 ± 0.20	…	…
IRAS 04579+4703	1	Y	05 01 40.05	+47 07 21.5	0.54 ± 0.09	0.44 ± 0.13	2.2 × 0.0	31
IRAS 18171−1548	1	Y	18 20 06.46	−15 46 39.9	0.66 ± 0.12	2.77 ± 0.62	14.3 × 9.1	127
IRAS 19045+0813	7	Y	19 07 00.59	+08 18 44.1	0.75 ± 0.05	1.10 ± 0.12	5.3 × 0.0	143
IRAS 20293+4007	2	Y	20 31 07.15	+40 17 28.1	0.55 ± 0.08	1.08 ± 0.22	6.1 × 3.1	76
IRAS 22187+5559	1	Y	22 20 31.87	+56 14 55.3	0.70 ± 0.05	1.32 ± 0.14	8.4 × 5.0	12
	2	Y	22 20 33.38	+56 15 06.8	1.13 ± 0.05	3.79 ± 0.22	13.2 × 8.8	179
	3	Y	22 20 33.72	+56 14 29.1	1.99 ± 0.05	17.33 ± 0.51	38.1 × 8.3	127
	4	Y	22 20 34.59	+56 15 00.4	1.95 ± 0.05	6.05 ± 0.21	11.2 × 9.3	99
	5	Y	22 20 35.64	+56 14 46.4	4.19 ± 0.05	19.31 ± 0.28	16.0 × 11.2	170
	1–5[c]	Y	…	…	4.64 ± 0.78	39.32 ± 1.34	…	…
IRAS 22198+6336	2	Y	22 21 26.87	+63 51 37.2	0.49 ± 0.04	1.11 ± 0.13	6.2 × 1.4	143
NGC 7538-IRS9	2	Y	23 14 01.10	+61 27 18.8	1.08 ± 0.20	1.43 ± 0.43	4.6 × 0.0	13
	3	Y	23 14 01.79	+61 27 20.0	2.12 ± 0.20	3.83 ± 0.52	4.4 × 1.8	14
IRAS 23448+6010	3	Y	23 47 20.61	+60 27 16.0	0.63 ± 0.08	0.80 ± 0.15	4.2 × 0.0	154

[a] Y = source within the central 50″ around the IRAS source; N = source out of the central 50″ around the IRAS source.
[b] Intensity and flux density corrected for primary beam response.
[c] Emission from the sources included in the range.

Table 8. Parameters of the sources detected at 7 mm.

Region	VLA source	Central source[a]	α(J2000.0) (h m s)	δ(J2000.0) (° ′ ″)	$I_\nu^{\text{peak}\, b}$ (mJy beam^{-1})	$S_\nu^{\ b}$ (mJy)	Deconv. Size (″)	PA (°)
IRAS 04579+4703	1	Y	05 01 40.01	+47 07 20.5	0.67 ± 0.08	1.45 ± 0.26	5.0 × 2.5	51
IRAS 19045+0813	7	Y	19 07 00.51	+08 18 44.3	0.58 ± 0.11	0.70 ± 0.20	3.1 × 0.0	31
IRAS 22187+5559[c]	3	Y	22 20 33.55	+56 14 31.7	1.09 ± 0.28	7.87 ± 0.48	…	…
	5a	Y	22 20 35.27	+56 14 36.2	1.10 ± 0.32	2.81 ± 0.51	8.1 × 2.7	30
	5b	Y	22 20 35.56	+56 14 45.4	1.42 ± 0.33	3.02 ± 0.63	6.6 × 2.8	110
	5c	Y	22 20 36.10	+56 14 41.7	0.99 ± 0.16	1.70 ± 0.66	6.7 × 4.8	5
	5d	Y	22 20 36.27	+56 14 38.1	1.07 ± 0.25	1.71 ± 0.59	4.6 × 3.2	140
	5a–5d[d]	Y	…	…	1.42 ± 0.31	12.05 ± 0.48	…	…
IRAS 22198+6336	2	Y	22 21 26.76	+63 51 37.9	2.10 ± 0.26	2.76 ± 0.53	1.5 × 0.3	110

[a] Y = source within the central 50 ″ around the IRAS source.
[b] Intensity and flux density corrected for primary beam response.
[c] VLA 5a to VLA 5d are the subclumps found toward the position of VLA 5.
[d] Emission from the sources included in the range.

or UCH II regions, and in Table 10 we list their physical parameters. Note that the emission measure, electron density, and opacity are beam-averaged values, and due to our angular resolution of ~10″ at 3.6 cm, these values are affected by an important filling factor.

From Table 10, we can see that the underlying star exciting the UCH II region is in all cases an early-type B star. We note that in the estimation of the physical parameters we assumed that the emission is optically thin. This is supported by the spectral indices close to zero reported in Table 9 for almost all the sources, except for I04579, for which the estimation of the rate of ionizing photons is a lower limit (e.g., Keto et al. 2008), and thus the spectral type of the ionizing star is earlier than B2–B3. For almost all the regions, the bolometric luminosity derived from the centimeter emission (from the spectral type and following Panagia 1973) is lower than the IRAS bolometric luminosity estimated from the infrared emission. For I00117

and I22187 only we found the IRAS luminosity to be a factor of ≲2 smaller. However, in both cases the centimeter sources are resolved into different components when observed with higher angular resolution (see Sects. 4.2.1 and 4.2.7), the 3.6 cm flux and the derived luminosity (at least for these two sources) being an upper limit on the luminosity coming from the massive YSO. Thus, the IRAS luminosity seems to be enough to account for the centimeter emission by photoionization. We conclude that all the centimeter sources associated with the IRAS sources of our sample seem to trace a compact or UCH II region.

4.2. Comments on individual sources

4.2.1. IRAS 00117+6412

At 3.6 cm there is one source elongated roughly in the east-west direction, and at 1.3 cm the source splits into two components, with the northern one, VLA 3, nearly coincident with the peak

Table 9. Spectral indices of the central sources.

Region	VLA source	Spectral index[a] (21–3.6 cm)	Spectral index[b] (3.6–1.3 cm)	Nature[c]
IRAS 00117+6412	2–3[d]	>+0.13	+0.18 ± 0.20	UCH II
IRAS 04579+4703	1	>−0.2	+1.1 ± 0.4[e]	UCH II/radiojet
IRAS 18123−1203	2	. . .	<+0.9[e]	
	4	. . .	<+0.8[e]	
	5	. . .	<−0.4[e]	
	6	. . .	<−0.1[e]	
	2–6[d]	>+0.17	. . .	
IRAS 18171−1548	1	>−0.3	−0.3 ± 0.2	compact H II
IRAS 19045+0813	2	. . .	<+1.1[e]	
	3	. . .	<+0.0[e]	
	4	. . .	<−0.3[e]	
	5	. . .	<+0.3[e]	
	6	. . .	<−0.2[e]	
	2–6[d]	>−0.03[f]	. . .	
	7	>+0.3	+0.4 ± 0.2	UCH II / radiojet
IRAS 20293+4007	1	. . .	<−0.8	
	2	. . .	+0.1 ± 0.2	compact H II
	1–2[d]	>−0.2	. . .	
IRAS 22187+5559	1	. . .	−0.3 ± 0.2[e]	ext. ionized?
	2	. . .	+0.14 ± 0.13[e]	ext. ionized?
	3	. . .	+0.0 ± 0.3	compact H II
	4	. . .	+0.6 ± 0.5	ext. ionized?
	5	. . .	−0.06 ± 0.17	compact H II
	1–5[d]	+0.04 ± 0.02	+0.13 ± 0.09	
IRAS 22198+6336	2	+0.5 ± 0.2[g]	+0.5 ± 0.3	UCH II/radiojet
NGC 7538-IRS9	2	. . .	>−1.2[e]	UCH II/radiojet
	3	. . .	>+0.1[e]	UCH II/radiojet
	2–3[d]	>−0.9[f]	. . .	
IRAS 23448+6010	1	. . .	<−0.2	UCH II
	2	. . .	<−0.2	UCH II
	3	. . .	>−0.1	UCH II
	4	. . .	<+1.2[e]	
	5	. . .	<+0.8[e]	
	6	. . .	<+0.9[e]	
	1–6[d]	>+0.2	. . .	

[a] Spectral index estimated from the flux density values at 21 cm from the NVSS (Condon et al. 1998) and at 3.6 cm (present work) obtained with the uv-range common to both wavelengths, 1–5 kλ. In the case of non-detection at one of the frequencies, an upper limit of 4 times the rms noise of the map was used.

[b] Spectral index estimated from the flux density values at 3.6 cm and 1.3 cm (present work) obtained with the uv-range common to both wavelengths, 4–25 kλ. In the case of non-detection at one of the frequencies, an upper limit of 4 times the rms noise of the map was used.

[c] See main text.

[d] Emission from the sources included in the range.

[e] Non-detection at 3.6 cm and 1.3 cm in the same uv-range maps. Flux density at 3.6 cm or 1.3 cm from Tables 6 or 7. Upper limits at 3.6 cm or 1.3 cm (for the case of extended sources) as $4A^{0.80}$ times the rms of the map (from Tables 2 or 3), with $A = 1 + \Omega_s/\Omega_b$, where Ω_s is the solid angle of the source at the frequency where it is detected, and Ω_b is the beam solid angle (see Beltrán et al. 2001).

[f] Non-detection at 21 cm and 3.6 cm in the same uv-range maps. Flux density at 3.6 cm for I19045 from Table 6, and flux density at 3.6 cm of 0.76 ± 0.15 mJy for NGC 7538-9 from Sandell et al. (2005).

[g] Flux density at 21 cm of 0.23 ± 0.05 mJy from the VLA archive data. See Sect. 3.4.

at 3.6 cm (Fig. 1). The millimeter emission has the main peak located ~15″ to the west of VLA 3 and shows a rather circular structure with some subcondensations. There are two H$_2$O masers close to the main and the secondary millimeter peaks (Cesaroni et al. 1988), suggesting that these two peaks are tracing embedded YSOs, and there is also outflow emission centered around the secondary millimeter peak (Zhang et al. 2005; Kim & Kurtz 2006). Observations with higher angular resolution at 3.6 cm (Busquet et al., in prep.) reveal no emission at the position of VLA 2, and that the source detected in this work at 3.6 cm

consists of two components. One component is associated with VLA 3 and with the brightest K-band infrared source in the region, which has some infrared excess, and the other is coincident with the main millimeter peak (likely harboring a deeply embedded intermediate mass YSO). Thus, VLA 3 is most likely a UCH II region at the border of a dusty cloud where active star formation is taking place. The SED of I00117 can be fitted for temperatures between 26 and 30 K, and for masses between 21 and 30 $M_\odot$, which are among the median values of all the sources in this survey.
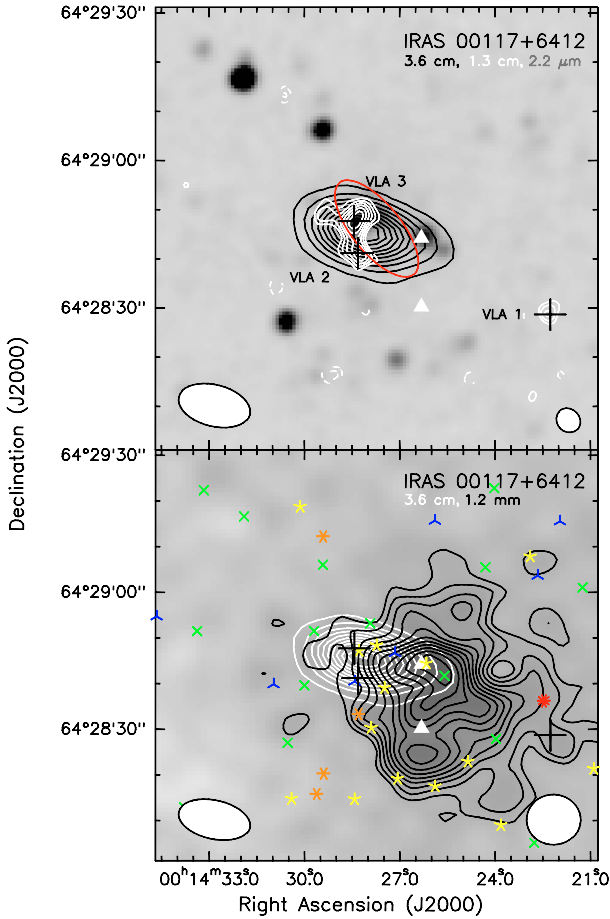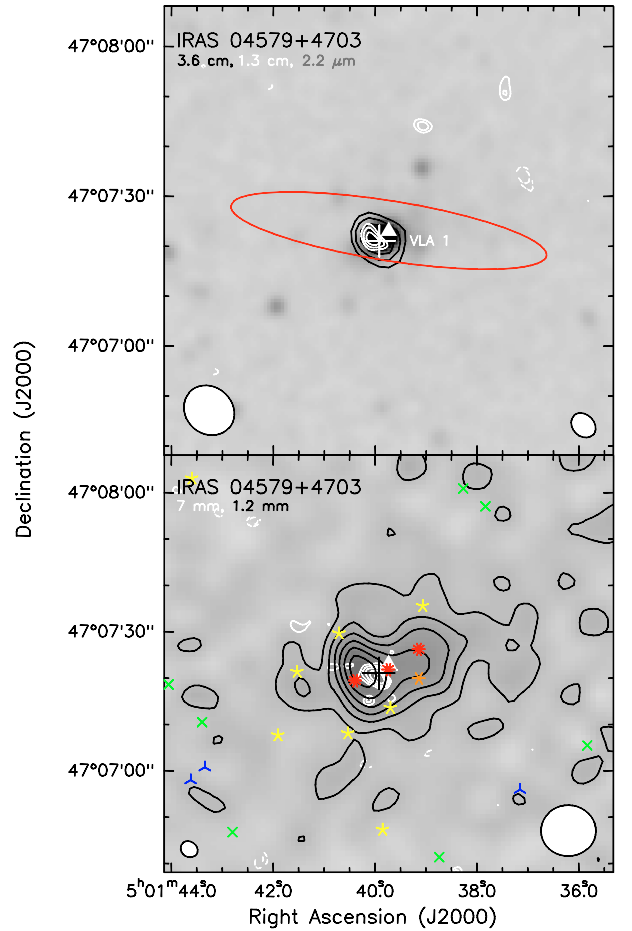
Fig. 1. IRAS 00117+6412. *Top*: black contours: VLA 3.6 cm continuum emission. Levels are −6, −3 and 3 to 33 in steps of 3, times 0.038 mJy beam^{-1}. White contours: VLA 1.3 cm continuum emission. Levels are −4, −3, 3, to 8 in steps of 1, times 0.067 mJy beam^{-1}. Grey scale: K-band 2MASS image. *Bottom*: grey scale and black contours: IRAM 30 m continuum emission at 1.2 mm. Levels are 3 to 13 in steps of 1, times 8 mJy beam^{-1}. White contours: 3.6 cm emission as in the top panel. Symbols in Figs. 1 to 10 are described here. A red ellipse indicates the error ellipse of the IRAS source. White and/or black crosses indicate the centimeter sources from Tables 6, and 7. White filled circles indicate CH$_3$OH masers, white filled triangles H$_2$O masers, and white filled squares OH masers. Color stars indicate 2MASS sources with the color and symbol corresponding to different infrared excess as described in Sect. 3.3. Synthesized beams at the bottom-left corners correspond to the first wavelength indicated at the top of the panel, and beams at the bottom-right corners, when available, correspond to the second wavelength at the top of the panel.

4.2.2. IRAS 04579+4703

The 3.6 cm source in this region is elongated in the southwest-northeast direction and has a counterpart at 1.3 cm, elongated also in the same direction. The spectral index, ∼ 1, indicates that the emission is thermal and partially thick. Such a spectral index has been found for thermal radiojets associated with sources powering molecular outflows (e.g., Beltrán et al. 2001; Zapata et al. 2004; Gibb & Hoare 2007), and for hypercompact H II regions (e.g., Carral et al. 1997; Ignace & Churchwell 2004; Kurtz 2005). There is an infrared source with strong infrared excess associated with the centimeter source, suggesting that the massive YSO is likely surrounded by circumstellar material (see Fig. 2). In addition, the dust continuum emission at 1.2 mm consists of a main condensation whose peak is clearly associated with the

Fig. 2. IRAS 04579+4703. *Top*: black contours: VLA 3.6 cm continuum emission. Levels are −4, −3 and 3 to 7 in steps of 1, times 0.022 mJy beam^{-1}. White contours: VLA 1.3 cm continuum emission. Levels are −4, −3, 3, to 5 in steps of 1, times 0.085 mJy beam^{-1}. Grey scale: K-band 2MASS image. *Bottom*: grey scale and black contours: IRAM 30 m continuum emission at 1.2 mm. Levels are 2 to 12 in steps of 2, times 7 mJy beam^{-1}. White contours: VLA 7 mm continuum emission. Levels are −4, −3, 3, to 7 in steps of 1, times 0.094 mJy beam^{-1}. Color stars indicate 2MASS sources and white filled symbols refer to masers (see Fig. 1, for more details).

centimeter source (the offset is <5″, the positional uncertainty of the IRAM 30 m), as well as with H$_2$O maser and NH$_3$ emission (Palla et al. 1991; Molinari et al. 1996). The spatial coincidence of the millimeter peak with the centimeter source suggests that the underlying massive star is in a very young evolutionary stage, not yet having pushed away the surrounding material. This is reinforced by the detection of a compact source at 7 mm at the position of the centimeter source. Note that 38% of the 7 mm flux density comes from the dust emission from the envelope/disk associated with the massive YSO, and for this dust component we estimated a mass of ∼13 $M_\odot$. Note also that the 7 mm emission, similar to the 3.6 and 1.3 cm emission, is slightly elongated in the southwest-northeast direction. Regarding the outflow emission, Zhang et al. (2005) detect no CO (2−1) outflow in the region using the NRAO 12 m Telescope. However, CO (1−0) emission previously had been detected using the IRAM 30 m with a linewidth of 6.1 km s^{-1} by Wouterloot & Brand (1989), with a sensitivity similar to that achieved by Zhang et al. (2005). Further sensitive observations are required to confirm or disprove the presence of an outflow associated with the massive YSO, and thus to properly interpret the nature of the elongated
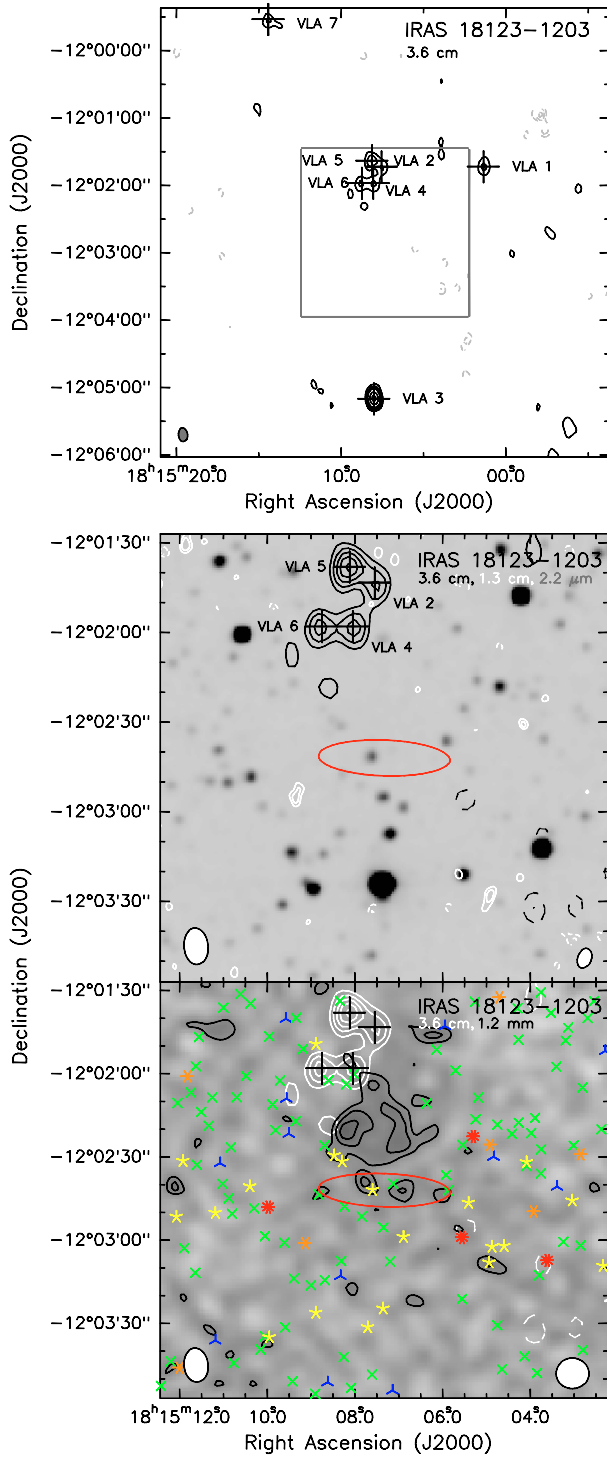
Fig. 3. IRAS 18123−1203. *Top*: VLA 3.6 cm map. The box shows the region zoomed in the other panels. *Middle*: black contours: VLA 3.6 cm continuum emission. Levels are −4, −3 and 3 to 7 in steps of 1, times 0.043 mJy beam^{-1}. White contours: VLA 1.3 cm continuum emission. Levels are −4, −3, 3, and 4, times 0.063 mJy beam^{-1}. Grey scale: *K*-band 2MASS image. *Bottom*: grey scale and black contours: IRAM 30 m continuum emission at 1.2 mm. Levels are 2 to 5 in steps of 1, times 15 mJy beam^{-1}. White contours: 3.6 cm emission as in the *middle panel*. Color stars indicate 2MASS sources and white filled symbols refer to masers (see Fig. 1, for more details).

emission at 7 mm. The values for the dust temperature and mass derived from the SED fit are around 30 K and 23 $M_{\odot}$, which are near the median values derived for the sources of this work.

There are 2MASS sources showing infrared excess, surrounding the centimeter source and falling within the millimeter condensation (see Fig. 2), indicating that a cluster of low mass YSOs is possibly forming around the massive YSO.

4.2.3. IRAS 18123−1203

We detected four sources toward I18123 at 3.6 cm within the central 50″, as well as a dust condensation consisting of different peaks (see Fig. 3). However, neither the centimeter emission nor the main millimeter emission are coincident with the IRAS source, and the centimeter and millimeter emissions are not overlapping. In addition, there are no 2MASS sources associated with the main dust condensation or the centimeter sources (except maybe for VLA 4). About 10″ to the south of the main dust condensation there is a faint and compact millimeter source at 3σ, associated with a 2MASS source with some infrared excess, and within the IRAS error ellipse. The faint *JHK* magnitudes of this 2MASS source, its marginal detection at 1.2 mm, and the non-detection of NH$_3$ emission toward the region (Molinari et al. 1996) suggest that the YSO associated with the IRAS source should be of low mass. However, this is in conflict with the assumed IRAS bolometric luminosity of 7900 $L_{\odot}$. Thus, either this object is peculiar, or its distance is overestimated.

The spatial anticorrelation between the centimeter and the millimeter emission is somewhat puzzling. We first considered the possibility that the centimeter emission is tracing externally ionized gas, and searched the catalog of Reed (2003)[3] for nearby OB stars. We did not find any OB star to the northeast of the centimeter emission which could account (following Lefloch et al. 1997) for the total centimeter flux of VLA 2, VLA 4 to VLA 6 (1.6 mJy), and thus we ruled out the possibility that these centimeter sources were externally ionized globules. Another possibility is that the centimeter emission traces extragalactic objects, suggested by the double radio source morphology. However, there are no sources detected at 21 cm in the NVSS (the spectral index between 21 and 3.6 cm being typical of thermal emission), and the spectral indices between 3.6 and 1.3 cm do not disprove a free-free thermal nature for the centimeter emission (except for VLA 5). Thus, the centimeter emission to the north of the IRAS source could be produced by a group of low mass YSOs driving thermal radiojets, whose extended emission may have been resolved out at 1.3 cm.

4.2.4. IRAS 18171−1548

The centimeter source, detected at 3.6 and 1.3 cm, has a flat spectral index, a size of ~0.15 pc, and is clearly associated with an infrared source detected in the *JHK* bands from 2MASS and revealed by the IRAC-*Spitzer* images at 3.6−8.0 μm as a bright nebulosity (but with no point source) emerging from a dark structure (Kumar & Grave 2007). Thus, the centimeter source is most likely tracing a compact H II region. Note that the compact H II region lies in a zone with a low density of infrared sources (see the 2MASS *K*-band image in Fig. 4), whose central part coincides with the dark structure revealed by IRAC. Note also that the IRAS source is slightly shifted to the west of the compact H II region, and has a 2MASS source with a strong associated infrared excess. The parameters derived for the compact H II region suggest that the underlying star is a B1 star, and

---

[3] Catalog available at http://othello.alma.edu/~reed/OBfiles.doc
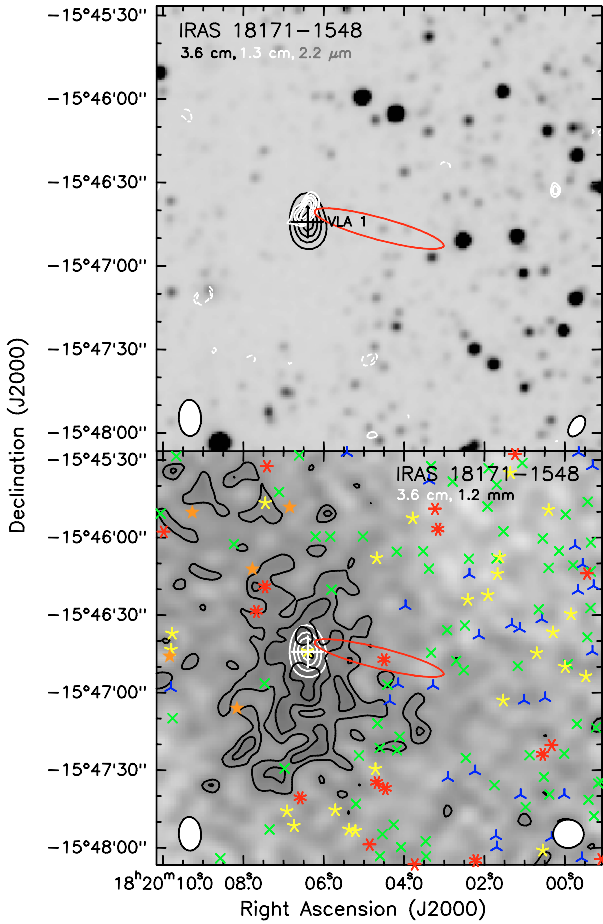
Fig. 4. IRAS 18171−1548. *Top*: black contours: VLA 3.6 cm continuum emission. Levels are −5, −3 and 3 to 9 in steps of 2, times 0.185 mJy beam^{-1}. White contours: VLA 1.3 cm continuum emission. Levels are −4, −3, 3, to 6 in steps of 1, times 0.112 mJy beam^{-1}. Grey scale: K-band 2MASS image. *Bottom*: grey scale and black contours: IRAM 30 m continuum emission at 1.2 mm. Levels are 2 to 5 in steps of 1, times 16 mJy beam^{-1}. White contours: 3.6 cm emission as in the top panel. Orange filled stars indicate IRAC-*Spitzer* sources classified as Class 0/I sources (see Sect. 3.3), and with no 2MASS counterpart. Color stars indicate 2MASS sources and white filled symbols refer to masers (see Fig. 1, for more details).

from the fit to the SED we estimated a mass of the envelope of around 100 $M_\odot$ for dust temperatures of ~28 K. The morphology revealed by the large-scale millimeter emission shows an elongated and clumpy condensation in the north-south direction coinciding with the zone with a small number of 2MASS sources. Thus, the millimeter emission seems to trace the cloud of dense gas and dust in which the massive star was formed, which is the most massive cloud of this survey, as derived from the flux density at 1.2 mm. The main dust condensation contains multiple peaks or subcondensations. Interestingly, the millimeter emission shows two peaks separated by ~15″, with the compact H II region lying in between them. This suggests that the compact H II region is pushing out the surrounding material toward the north and south, disrupting the cloud and decreasing its density. This could explain why no NH$_3$ (Molinari et al. 1996), and CS (2−1) (Bronfman et al. 1996) has been detected toward the region.

4.2.5. IRAS 19045+0813

The centimeter emission toward I19045 presents two main components (see Fig. 5), the UCH II region candidate, and a
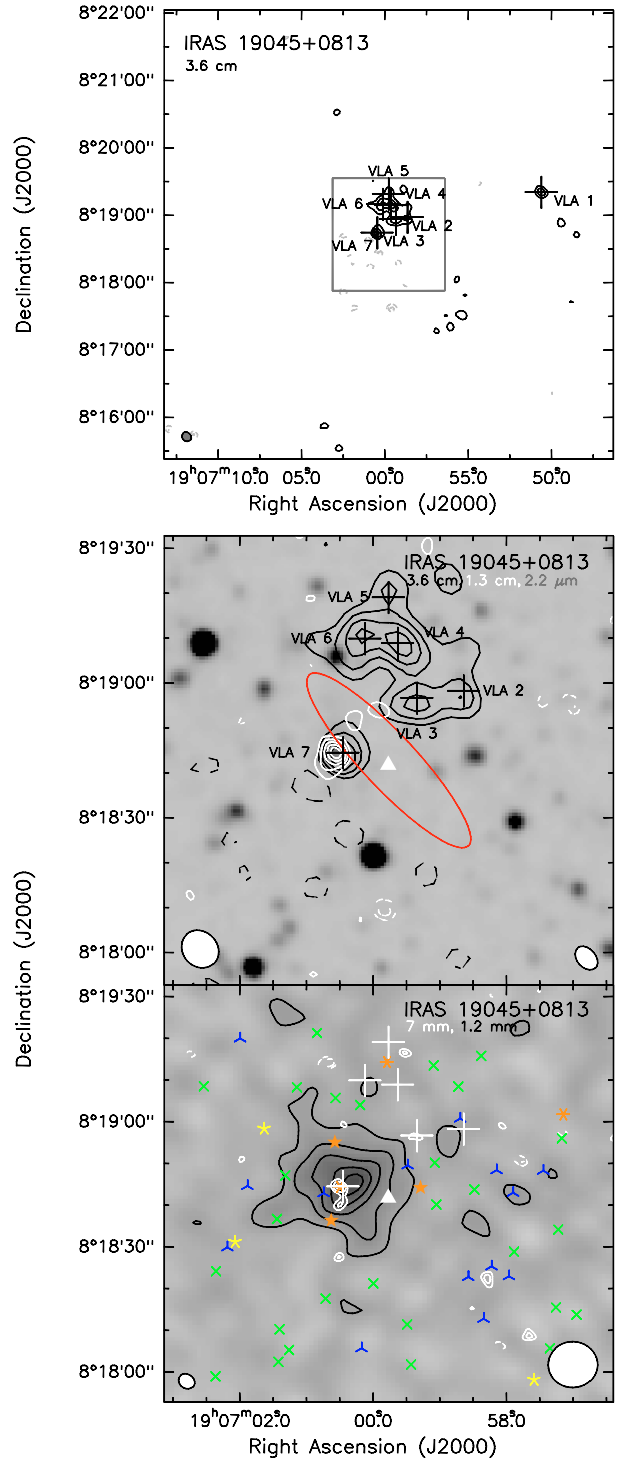
Fig. 5. IRAS 19045+0813. *Top*: VLA 3.6 cm map. The box shows the region zoomed in the other panels. *Middle*: black contours: VLA 3.6 cm continuum emission. Levels are −5, −3 and 3 to 11 in steps of 2, times 0.054 mJy beam^{-1}. White contours: VLA 1.3 cm continuum emission. Levels are −5, −3, 3 to 11 in steps of 2, times 0.065 mJy beam^{-1}. Grey scale: K-band 2MASS image. *Bottom*: grey scale and black contours: IRAM 30 m continuum emission at 1.2 mm. Levels are 2 to 10, in steps of 2, times 9 mJy beam^{-1}. White contours: VLA 7 mm continuum emission. Levels are −4, −3 and 3 to 5 in steps of 1, times 0.100 mJy beam^{-1}. Color (orange filled) stars indicate 2MASS (IRAC-Spitzer) sources and white filled symbols refer to masers (see Figs. 1 and 4, for details).

second component with extended emission to the northwest of the UCH II region. The UCH II region, falling within the IRAS

Table 10. Physical parameters of the H II regions.

Region	VLA source	ν (GHz)	Diameter (pc)	T_B (K)	$f\,EM^a$ (10^3 cm^{-6} pc)	$f\,n_e{}^a$ (10^3 cm^{-3})	$M_i{}^b$ ($M_\odot$)	$\dot{N}_i$ (s^{-1})	Spectral type[c]
IRAS 00117+6412	2–3	8.5	0.054	0.82	22.3	0.64	1.3×10^{-3}	3.8×10^{44}	B2
IRAS 04579+4703	1	8.5	<0.040	>0.27	>7.2	>0.42	$<1.9 \times 10^{-3}$	6.8×10^{43}	B2–B3
IRAS 18171−1845	1	8.5	0.139	0.56	14.8	0.33	1.8×10^{-2}	1.7×10^{45}	B1
IRAS 19045+0813	7	8.5	0.026	1.02	27.1	1.01	9.8×10^{-4}	1.1×10^{44}	B2–B3
IRAS 20293+4007	2	8.5	0.158	0.43	11.8	0.27	1.9×10^{-2}	1.7×10^{45}	B1
IRAS 22187+5559	3	8.5	0.287	1.53	40.8	0.38	1.2×10^{-1}	2.0×10^{46}	B0.5
	5	8.5	0.243	2.51	66.9	0.53	1.1×10^{-1}	2.3×10^{46}	B0.5
IRAS 22198+6336	2	8.5	<0.010	>4.97	>132.0	>3.74	$<6.4 \times 10^{-4}$	7.0×10^{43}	B3
NGC 7538-IRS9	2	22.5	<0.062	>0.18	>39.1	>0.79	$<1.9 \times 10^{-3}$	9.0×10^{44}	B1–B2
	3	22.5	0.038	1.27	279.0	2.70	4.0×10^{-3}	2.4×10^{45}	B1
IRAS 23448+6010	1	8.5	<0.129	>0.06	>1.7	>0.11	$<3.1 \times 10^{-3}$	1.6×10^{44}	B2–B3
	2	8.5	0.173	0.12	3.1	0.14	9.0×10^{-3}	5.5×10^{44}	B2
	3	22.5	<0.041	>0.12	>25.9	>0.80	$<7.0 \times 10^{-3}$	2.6×10^{44}	B2

[a] f corresponds to the filling factor.
[b] Mass of ionized gas estimated from the beam averaged electron density and the observed size of the source.
[c] Estimated from Panagia (1973).

Table 11. Parameters of the Spectral Energy Distribution fits, and dust thermal emission at 1.2 and 7 mm.

Region	VLA source	free-free Spectral index	β	T (K)	M ($M_\odot$)	1.2 mm M^a ($M_\odot$)	7 mm Dust emission $S_\nu{}^b$ (mJy)	7 mm Dust emission M^c ($M_\odot$)
IRAS 00117+6412	2–3[d]	+0.18	1.5–1.7	30–26	21–30	36		
IRAS 04579+4703	1	+1.1	1.8–2.0	32–28	20–26	23	0.5 ± 0.4	8–19
IRAS 18171−1548	1	−0.3	1.7–2.0	30–26	100–170	142		
IRAS 19045+0813	7	+0.4	1.9–2.2	29–26	8–12	10	. . .	. . .
IRAS 22187+5559	3	+0.0	1.9–2.1	34–32	10–20	14	. . .	. . .
	5	−0.06	1.9–2.0	32–31	30–40	32	. . .	. . .
IRAS 22198+6336	2	+0.5	1.7–1.9	29–25	20–30	20[e]	1.2 ± 0.7	6–11
NGC 7538-IRS9	2–3[d]	−0.10[f]	1.9–2.0	35–32	50–80	66[g]		

[a] Dust and gas mass from IRAM 30 m 1.2 mm observations (Table 5).
[b] Flux density at 7 mm without the free-free contribution estimated from the 3.6 and 1.3 cm emissions.
[c] Dust and gas mass from the 7 mm dust emission, assuming a dust temperature in the 50–100 K range (Gómez et al. 2003), a dust emissivity index of 2 and a dust mass opacity coefficient of 0.9 cm^2 g^{-1} at 1.2 mm (Ossenkopf & Henning 1994). The higher value corresponds to a temperature of 50 K, and the lower to a temperature of 100 K.
[d] Emission from the sources included in the range.
[e] Estimated from the 850 μm flux density from Jenness et al. (1995).
[f] Value adopted for the SED fit, due to the detection of the source at only one wavelength.
[g] Estimated from the 1.2 mm flux density from Sandell & Sievers (2004).

error ellipse, is associated with a 2MASS source with infrared excess and with an IRAC-*Spitzer* source (Kumar & Grave 2007) classified as a Class 0/I source from the K−[3.6] vs. [3.6]−[4.5] and [3.6]−[4.5] vs. [4.5]−[5.8] diagrams (Sect. 3.3). There is CS (2−1) (Bronfman et al. 1996) and H$_2$O maser emission (Palla et al. 1991) detected in the region. The 1.2 mm continuum emission is associated with the UCH II region, with three IRAC sources classified as Class 0/I (Sect. 3.3), and with faint emission at 7 mm. The 7 mm emission has a secondary peak toward the south, in the same direction as the extension seen in the 1.3 cm emission. The 7 mm emission does not seem to have a contribution from thermal dust emission; therefore, the centimeter emission, up to 7 mm, is most likely tracing an ionized wind, as suggested by the spectral index of 0.2–0.6. The dust temperature derived from the SED, 26–29 K, is similar to the median value of the survey, and the associated mass is the smallest, around 8−12 $M_\odot$.

The extended centimeter emission to the northwest consists of a curved structure with different subcomponents, VLA 2 to VLA 6, and is not overlapping with the millimeter emission, but starts when the millimeter emission finishes. This is reminiscent of a bright-rimmed cloud, as the centimeter emission follows the border of the dust cloud. We searched the catalog of Reed (2003) for nearby OB stars to the northwest of the millimeter emission, and the closest star was a B2.5 star at ~2.5° to the north-west (70 pc), which is too far away to account for the flux of VLA 2 to VLA 6, following Lefloch et al. (1997). Given the double lobe morphology and the negative spectral indices of some of these sources (see Fig. 5 and Table 9), they could be tracing extragalactic objects. However, there are no sources detected at 21 cm in the NVSS, and we estimated a lower limit for the spectral index of VLA 2 to VLA 6 between 21 and 3.6 cm of >−0.03 (see Table 9), typical of thermal emission. Thus, we favor the interpretation that these sources are
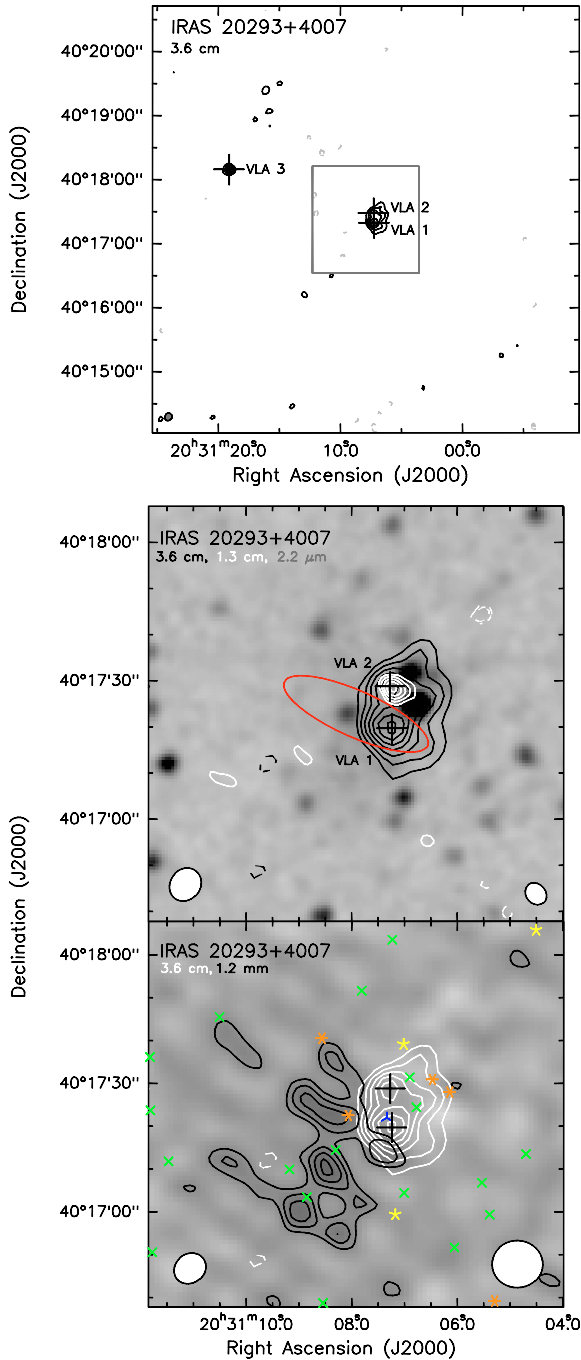
Fig. 6. IRAS 20293+4007. *Top*: VLA 3.6 cm map. The box shows the region zoomed in the other panels. *Middle*: black contours: VLA 3.6 cm continuum emission. Levels are −5, −3 and 3 to 15 in steps of 2, times 0.058 mJy beam^{-1}. White contours: VLA 1.3 cm continuum emission. Levels are −4, −3, and 3 to 7 in steps of 1, times 0.080 mJy beam^{-1}. Grey scale: *K*-band 2MASS image. *Bottom*: grey scale and black contours: IRAM 30 m continuum emission at 1.2 mm. Levels are 3 to 6 in steps of 1, times 9 mJy beam^{-1}. White contours: 3.6 cm emission as in the *middle panel*. Color stars indicate 2MASS sources (see Fig. 1, for more details).

thermal, and have not been detected at 1.3 cm because their emission is extended and thus (partially) resolved out by the interferometer.

4.2.6. IRAS 20293+4007

At 3.6 cm, I20293 is dominated by one strong source (see Fig. 6). This source has two subcomponents, VLA 1 (south) and VLA 2 (north), and the centimeter peaks are not clearly associated with any 2MASS source, although a few fall within the extended centimeter emission. At 1.3 cm there is one strong source slightly resolved at the position of VLA 2. The spectral index suggests that VLA 2 is a thermal source, and is likely tracing the UCH II region associated with the IRAS source. However, the IRAS source could be also associated with a 2MASS source showing infrared excess that falls just at the eastern edge of the centimeter emission. The emission at 1.2 mm is extended and clumpy, and shifted to the east with respect to the centimeter emission (similarly to I00117). There is no millimeter emission directly associated with the centimeter emission, suggesting that the UCH II region (possibly VLA 2) has disrupted and pushed the surrounding gas away. Again this could be the reason why NH$_3$ is not detected in the region (Molinari et al. 1996).

4.2.7. IRAS 22187+5559

I22187 contains the most extended centimeter source of this survey (see Fig. 7). The morphology of the centimeter emission reveals two main subcomponents, encompassed by a common structure extending toward the northwest. The strongest subcomponent, VLA 5, located in the north, is compact, has an extension toward the northwest and could be associated with a 2MASS source (with no infrared excess) lying at about 3″ to the northwest of the centimeter peak. The second subcomponent, VLA 3, fainter and located to the south, is elongated in the southeast-northwest direction. At 1.3 cm, the emission strongly resembles the 3.6 cm emission, with three faint additional components within the extended emission, VLA 1 to the north of VLA 3, and VLA 2 and VLA 4 to the northwest of VLA 5. The spectral index of VLA 3 and VLA 5 is flat for both sources, while for the three faint sources, the spectral index varies from flat to +0.6. These three faint sources could be globules externally ionized by VLA 3 and VLA 5. Garay et al. (2006) find in IRAS 16128−5109 a similar case of centimeter emission coming from externally ionized globules.

The large-scale 1.2 mm emission also presents two main condensations, which are slightly (∼7″) displaced from VLA 5 (millimeter peak to the east) and VLA 3 (millimeter peak to the south). The 1.2 mm emission is likely associated with the HCO$^+$ emission (Richards et al. 1987) and the CO emission detected in the region (Wouterloot & Brand 1989). SCUBA maps at 850 and 450 μm (Di Francesco et al. 2008) show condensations associated with the 1.2 mm peaks (see Fig. 7). We estimated a flux density of 0.7 ± 0.2 Jy at 850 μm and 6.1 ± 2.2 Jy at 450 μm for the condensation associated with VLA 3, and a flux density of 1.9 ± 0.2 Jy at 850 μm and 12.0 ± 2.9 Jy at 450 μm for the condensation associated with VLA 5. In the mid-infrared there are two MSX sources whose morphology and position are very similar to the two 1.2 mm, 850 μm, and 450 μm condensations. In addition, the POSSII red plates reveal a zone of high extinction starting at the position of VLA 5 and extending to the east, which matches the MSX and 1.2 mm sources (see Fig. 7). Another zone of high extinction is also found to the south of VLA 3 (see Fig. 7). These high extinction zones, traced by the millimeter and mid-infrared emissions, are likely tracing a dense molecular cloud seen against a bright background. We note that while VLA 3 is associated with optical emission, VLA 5 lies within the molecular cloud (dark in the optical), and thus seems to be
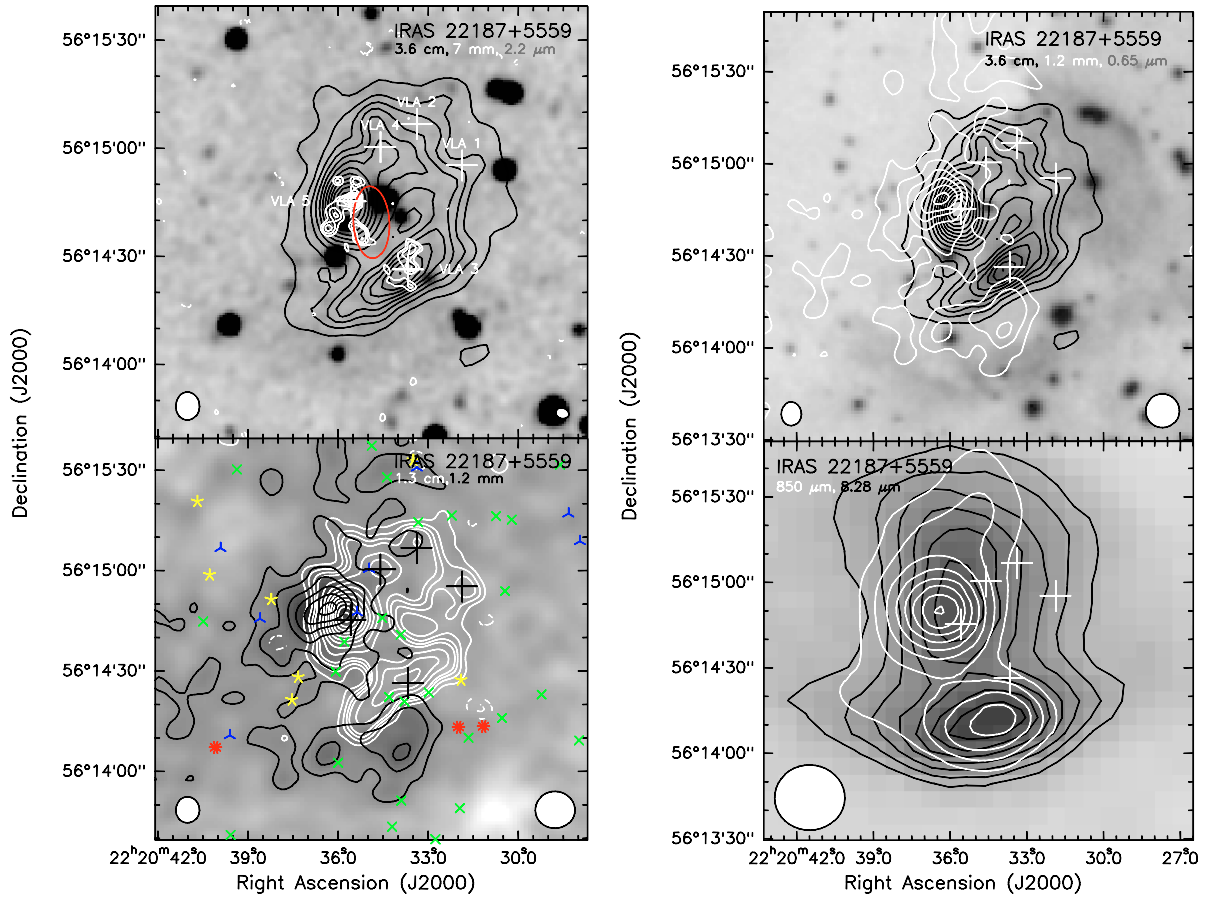
Fig. 7. IRAS 22187+5559. *Top-left*: black contours: VLA 3.6 cm continuum emission. Levels are −5, −3 and 3 to 42 in steps of 3, times 0.155 mJy beam^{-1}. White contours: VLA 7 mm continuum emission. Levels are −4, −3, and 3 to 9 in steps of 1, times 0.178 mJy beam^{-1}. Grey scale: *K*-band 2MASS image. *Bottom-left*: grey scale and black contours: IRAM 30 m continuum emission at 1.2 mm. Levels are 2 to 12 in steps of 2, times 7 mJy beam^{-1}. White contours: VLA 1.3 cm continuum emission. Levels are −5, −3, 3, 5, 7 and 12 to 75 in steps of 7, times 0.060 mJy beam^{-1}. *Top-right*: grey scale: POSS-II red image. Black contours: 3.6 cm emission as in the *top-left panel*. White contours: 1.2 mm emission as in the *bottom-left panel*. *Bottom-right*: grey scale and black contours: *A*-band MSX image (8.28 μm). White contours: SCUBA 850 μm emission. Levels are 3 to 17 in steps of 2, times 0.045 Jy beam^{-1} (Di Francesco et al. 2008). Color stars indicate 2MASS sources (see Fig. 1, for more details).

more embedded and probably younger than VLA 3. Note also that the extension of the centimeter emission toward the west of VLA 5 and VLA 3 is suggestive of the material surrounding the centimeter peaks having a lower density on the west side than on the east/southern sides, where the higher-density gas could be slowing down the expansion of the ionized gas.

A cluster of 7 mm sources is associated with both VLA 5 and VLA 3. The strongest 7 mm source, associated with VLA 5, is elongated in the east-west direction, is surrounded by different fainter 7 mm sources, and is possibly associated with the closest 2MASS source, which is shifted only 2″1. For VLA 3, the emission has several components with the strongest one located ~5″ to the north of the centimeter peak. All the 7 mm emission associated with VLA 3 and VLA 5 comes from thermal free-free emission. We built and fitted two different SEDs for VLA 3 and VLA 5, and obtained similar temperatures for both sources. The associated mass is higher for VLA 5 (~35 $M_\odot$) than for VLA 3 (~15 $M_\odot$).

4.2.8. IRAS 22198+6336

This source is located in the L1204/S140 molecular complex. Tafalla et al. (1993), using the CS(1−0) transition, detect seven cores in a region of ~50′, named A to G. L1204-G is

associated with I22198. (Note that some authors name I22198 as L1204-A, which has the coordinates of IRAS 22176+6303, so one must be cautious when using the labeling of Tafalla et al. 1993). Observations of CO and C^{18}O by Jenness et al. (1995) and observations of CO by Zhang et al. (2005) show evidence of molecular outflow emission. There is also H$_2$O maser emission detected by Palla et al. (1991), Tofani et al. (1995), Valdettaro et al. (2002) and Felli et al. (2007), who find several bursts of variable duration (200−500 days).

Emission at 3.6 cm shows a compact single source lying within the IRAS error ellipse (see Fig. 8), with a counterpart at 1.3 cm, but with no 2MASS or MSX sources associated. The centimeter peaks spatially coincide (~5″ to the northeast) with a strong and compact submillimeter condensation detected at 450 and 850 μm by Jenness et al. (1995). In addition, emission at 7 mm has been detected toward the source, with 44% of the flux at 7 mm coming from thermal dust emission. The mass of the 7 mm dust component is ~9 $M_\odot$. The source at 1.3 cm and 7 mm is elongated in the southeast-northwest direction (see Fig. 8 bottom panel), with a structure reminiscent of a radio-jet, consistent with the spectral index measured in the centimeter range, ~0.5. Furthermore, the large-scale outflow found in this region is slightly elongated in the southeast-northwest direction. However, since a substantial part of the 7 mm flux density comes
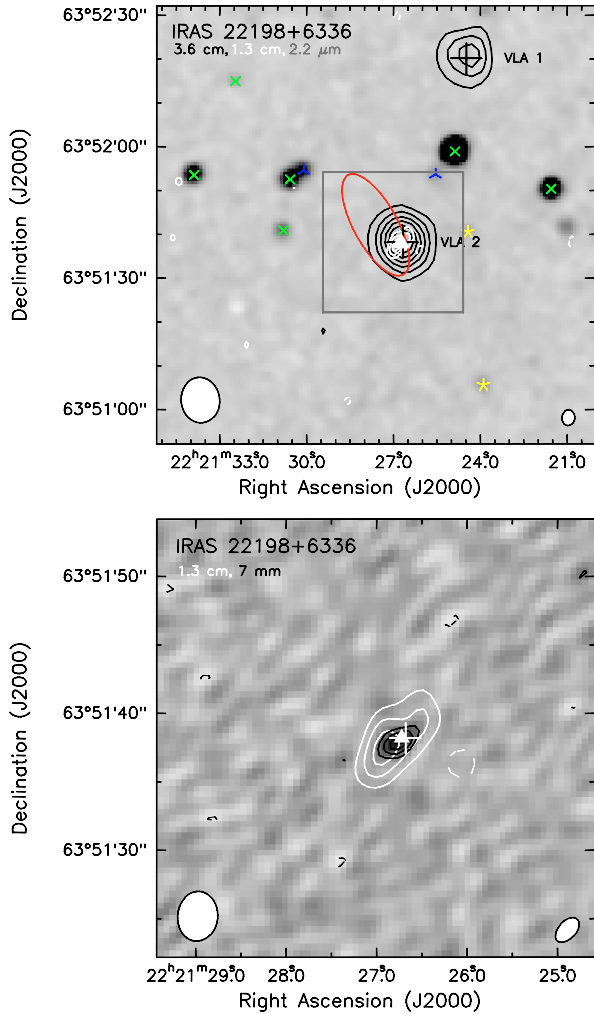
Fig. 8. IRAS 22198+6336. *Top*: black contours: VLA 3.6 cm continuum emission. Levels are -6, -3 and 3 to 21 in steps of 3, times 0.027 mJy beam^{-1}. White contours: VLA 1.3 cm continuum emission. Levels are -5, -3, and 3 to 9 in steps of 2, times 0.063 mJy beam^{-1}. Grey scale: *K*-band 2MASS image. The box shows the region zoomed in the *bottom panel*. *Bottom*: grey scale and black contours: VLA 7 mm continuum emission. Levels are -5, -3, and 3 to 7 in steps of 2, times 0.226 mJy beam^{-1}. White contours: 1.3 cm emission as in the top panel. Color stars indicate 2MASS sources and white filled symbols refer to masers (see Fig. 1, for more details).

from thermal dust emission, at this wavelength we are probably observing the superposition of an ionized wind and a dust disk. If the direction of the outflow is the same as the direction of the elongation of the 1.3 cm and 7 mm emissions, one could infer from the measured deconvolved size of the 7 mm source, 3250×260 AU, an upper limit for the size of the disk, ~ 300 AU, as the disk is expected to be perpendicular to the 7 mm source. It would be necessary to study the outflow with high angular resolution to confirm its direction and thus the upper limit for the size of the disk. As no near/mid-infrared sources are associated with the centimeter emission (note that there is no distance effect because this is the source of the survey with the shortest distance), this source must be deeply embedded in cold dust (as indicated by the derived dust temperature of $25-29$ K). We propose that VLA 2 is the youngest source of our survey and is tracing an early-type B protostar in an evolutionary stage similar to Class 0 sources in the low mass regime.

4.2.9. NGC 7538-IRS9

We detected one source at 1.3 cm (at 3.6 cm we were limited by dynamic range), associated with the IRAS source and with a 2MASS source at the northeastern border of an infrared nebulosity (see Fig. 9). The source at 1.3 cm splits into two subcomponents, VLA 2 and VLA 3, VLA 3 being clearly associated with the infrared source IRS 9.

NH$_3$ observations were carried out by Zheng et al. (2001), and CO and H$_2$ observations by Davis et al. (1998), who discovered an H$_2$ jet in the southeast-northwest direction. Sandell et al. (2005) detect three molecular outflows in the region: one HCO$^+$ high-velocity outflow associated with IRS 9 (VLA 3); another outflow associated with a protostellar core located $\sim 25''$ to the southeast of IRS 9; and a third outflow, detected in the CO (1$-$0) transition, coincident with the H$_2$ jet, whose driving source, according to Sandell et al. (2005), is traced by an infrared peak labeled "A1" by Tamura et al. (1991). This infrared peak coincides with the position of the VLA 2 peak. Thus, the centimeter source detected is probably the counterpart of the infrared source driving the H$_2$ jet. H$_2$O, OH, and CH$_3$OH maser emission has been detected (Kameya et al. 1990; Sandell et al. 2005) in IRS 9 and in the outflows.

The large-scale millimeter emission toward NGC 7538 has been studied by a number of authors. Reid & Wilson (2005) map the submillimeter continuum emission at 450 and 850 μm, and detect a single source at both wavelengths, clearly associated with IRS 9, with a faint extension to the south likely associated with the infrared nebulosity. Sandell & Sievers (2004) map the continuum emission at 350 μm and 1.3 mm, finding similar results.

The region was observed at 7 mm by van der Tak & Menten (2005) with the VLA in the C and A configurations. These authors detect one source at the position of VLA 3 (positions agree within $0.''3$), which is elongated in the north-south direction in the A-configuration observations. This is consistent with the deconvolved position angle that we have obtained toward VLA 3, $10°$. The present observations at 1.3 cm add a new point to the centimeter SED, which was fitted through an ionized accretion flow model by van der Tak & Menten (2005). Our value at 1.3 cm is about a factor of 2 higher than that predicted by the model (see Fig. 4 of van der Tak & Menten 2005), most likely because our observations were carried out in the D configuration and thus picked up more extended emission. The dust temperature from the SED fitted by us (which includes both VLA 2 and VLA 3) using a modified blackbody law, is near the median value of the survey, and the associated mass, $50-80\ M_\odot$, is among the highest in the survey. The small deconvolved size of the 1.3 cm source, its association with a 7 mm source (van der Tak & Menten 2005) and with the peak of a compact 1.3 mm source (Sandell & Sievers 2004), the high infrared excess of the 2MASS source associated with VLA 3, together with the fact that the centimeter fluxes are consistent with an ionized accretion flow (van der Tak & Menten 2005) suggest that VLA 3 (and probably VLA 2) is among the youngest sources in the survey.
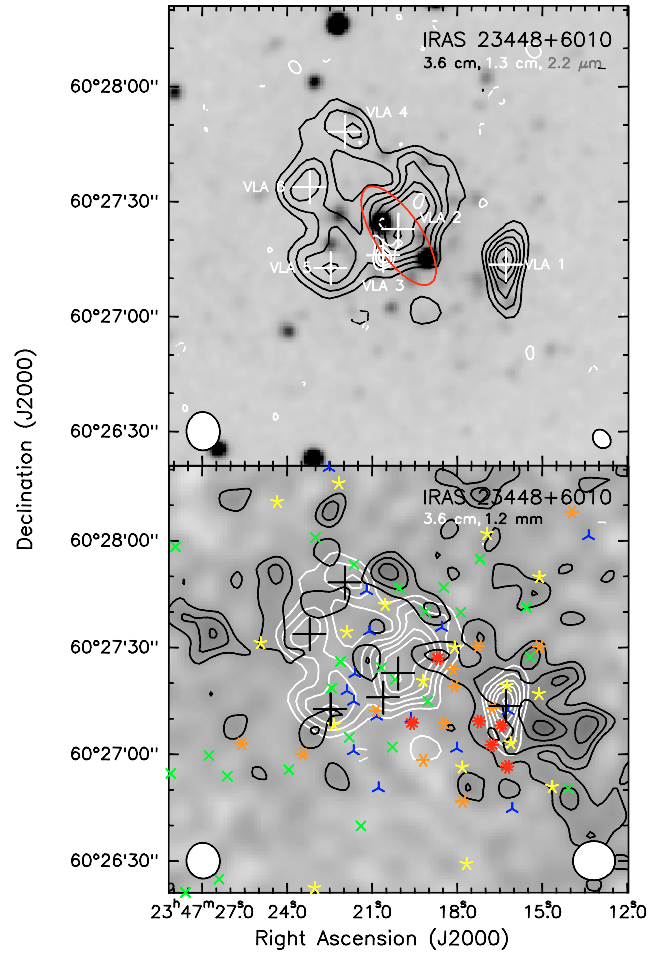
4.2.10. IRAS 23448+6010

The 3.6 cm emission toward this region shows a number of sources that lie in a region with a cluster of 2MASS sources showing strong infrared excess (Kumar et al. 2006, see Fig. 10). The 1.2 mm emission of the region is faint and extended and surrounds the northern and western edges of the centimeter emission. Three of the centimeter sources, VLA 1 to VLA 3, have
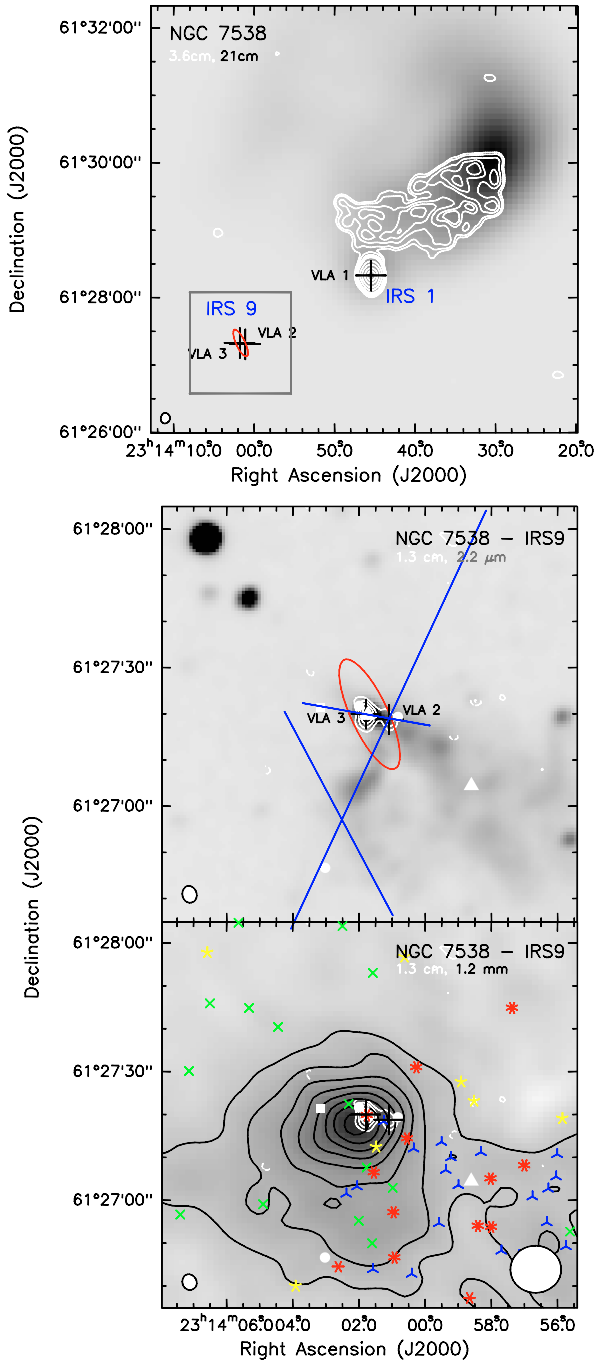
Fig. 9. NGC 7538-IRS9. *Top*: grey scale: 21 cm emission from NVSS. White contours: VLA 3.6 cm continuum emission. Levels are 3, 5, 10, 15, 20, 50, 100, 200, 300 and 400, times 1.28 mJy beam^{-1}. The box shows the region zoomed in the other panels. *Middle*: white contours: VLA 1.3 cm continuum emission. Levels are −5, −3 and 3 to 11 in steps of 2, times 0.204 mJy beam^{-1}. Grey scale: K-band 2MASS image. Blue lines correspond to molecular outflows (Sandell et al. 2005). *Bottom*: grey scale and black contours: IRAM 30 m continuum emission at 1.3 mm. Levels are 5 to 35 in steps of 3, times 30 mJy beam^{-1} (Sandell & Sievers 2004). White contours: 1.3 cm emission as in *middle panel*. Color stars indicate 2MASS sources and white filled symbols refer to masers (see Fig. 1, for more details).

spectral indices compatible with thermal free-free optically thin emission, and thus could be UCH II regions, although with different properties: while VLA 3 is the only centimeter source detected at 1.3 cm, and has no 2MASS counterpart, VLA 1 and

Fig. 10. IRAS 23448+6010. *Top*: black contours: VLA 3.6 cm continuum emission. Levels are −5, −3 and 3 to 13 in steps of 2, times 0.030 mJy beam^{-1}. White contours: VLA 1.3 cm continuum emission. Levels are −5, −3, 3, 5, and 7, times 0.076 mJy beam^{-1}. Grey scale: K-band 2MASS image. *Bottom*: grey scale and black contours: IRAM 30 m continuum emission at 1.2 mm. Levels are 2 to 5 in steps of 1, times 11 mJy beam^{-1}. White contours: 3.6 cm emission as in the bottom-left panel. Color stars indicate 2MASS sources (see Fig. 1, for more details).

VLA 2 are only detected at 3.6 cm and are clearly associated with 2MASS sources, with VLA 2 falling inside the IRAS error ellipse. As the 2MASS source coincident with VLA 2 is not detected in the J-band, we estimated its infrared excess from the $(H − K)$ color alone, which is 0.63, typical of T Tauri stars (e.g., Kenyon & Hartmann 1995), and thus included in the group of sources with infrared excess <0.4 (following Sect. 3.3). We note that the centimeter emission of VLA 2 to VLA 6 is reminiscent of a ring-like structure and that this emission could be produced by the ionizing photons from the UCH II regions. However, none of these sources lie at the center of the ring, and in addition, the rate of ionizing photons coming from VLA 2 or VLA 3 is too low (more than one order of magnitude) to produce the centimeter emission of VLA 4, VLA 5 and VLA 6 (following Lefloch et al. 1997). Thus, the centimeter emission of I23448 may be tracing a young cluster of B-type stars, which could be dispersing the surrounding material and would be responsible for the morphology of the millimeter emission. Garay et al. (2006) find a similar case of a cluster of centimeter sources in IRAS 15502−5302, but with the millimeter emission still associated with the centimeter sources. HCO$^+$ and HCN emission has been detected toward

Table 12. Evolutionary indicators of the sources, classified from smallest to largest disruption degree (see Sect. 4.3).

Region	VLA Source	cm Structure	cm-mm Offset (pc)	mm Structure	Disruption Degree[a] (%)	Dense Gas	Outflow	Maser Emission CH₃OH	H₂O	OH	2MASS IR Excess	MSX Emission
IRAS 22198+6336	3	disk / radiojet	≤0.03	compact[b]	7[b]	NH₃, CS	yes		yes	no	...[c]	no
IRAS 19045+0813	7	compact	≤0.04	compact	46	CS		no	yes	no	orange	yes
IRAS 04579+4703	1	compact	≤0.06	compact	56	NH₃	yes[d]	no	yes	no	red	yes
NGC 7538-IRS9	3	compact	~0.09	compact[b]	69[b]	NH₃, HCN	yes	yes	yes	yes	red	yes
IRAS 18171−1548	1	compact	~0.08	peak+ext	78	no		no	no	no	yellow	yes
IRAS 22187+5559	5	peak+ext	~0.10	peak+ext	78	HCO⁺	yes[d]		no	no	blue[e]	yes
IRAS 00117+6412	2–3	compact	~0.13	peak+ext	81	NH₃, CS	no[f]	no	yes	no	yellow	yes
IRAS 23448+6010	2	ext	~0.19	dispersed	82	HCN, HCO⁺			no	no	...[g]	yes
IRAS 22187+5559	3	peak+ext	~0.10	peak+ext	87	HCO⁺	yes[d]		no	no	green[e]	yes
IRAS 20293+4007	2	compact	~0.25	dispersed	91	no			no	no	green[e]	yes

[a] Defined in Eq. (1). The error of the disruption degree is ~4%.
[b] I22198 850 μm map from Jenness et al. (1995), and NGC 7538-IRS9 1.3 mm map from Sandell & Sievers (2004).
[c] Source not detected in the 2MASS catalog.
[d] Weak outflow emission.
[e] 2MASS sources falling inside the centimeter emission, but slightly offset from the centimeter peak.
[f] Outflow emission detected toward a source embedded in the dust condensation but not toward the centimeter source.
[g] See Sect. 4.2.10.
Note. The values of this table come from this work and from different references for each source. References for I00117: 4, 6, 14, 17, 29, 30; I04579: 7, 17, 27, 28, 29, 30; I18171: 4, 17, 19, 26; I19045: 3, 4; I20293: 17, 19; I22187: 7, 9, 19, 20, 29; I22198: 7, 8, 10, 12, 15, 17, 19, 23, 24, 25, 27, 29, 30, 32; NGC 7538-9: 2, 11, 13, 16, 21, 31; I23448: 5, 7, 18, 19, 20, 28, 29.
References: (1) Bachiller et al. (1990); (2) Boogert et al. (2002); (3) Brand et al. (1994); (4) Bronfman et al. (1996); (5) Casoli et al. (1986); (6) Cesaroni et al. (1988); (7) Edris et al. (2007); (8) Furuya et al. (2003); (9) Galt et al. (1989); (10) de Gregorio-Monsalvo et al. (2006); (11) Hasegawa & Mitchell (1995); (12) Jenness et al. (1995); (13) Kameya et al. (1990); (14) Kim & Kurtz (2006); (15) Larionov et al. (1999); (16) Mitchell & Hasegawa (1991); (17) Molinari et al. (1996); (18) Nguyen-Q-Rieu et al. (1987); (19) Palla et al. (1991); (20) Richards et al. (1987); (21) Sandell et al. (2005); (22) Slysh et al. (1994); (23) Tafalla et al. (1993); (24) Tofani et al. (1995); (25) Valdettaro et al. (2002); (26) van der Walt et al. (1995); (27) Wilking et al. (1989); (28) Wouterloot et al. (1993); (29) Wouterloot & Brand (1989); (30) Zhang et al. (2005); (31) Zheng et al. (2001); (32) Felli et al. (2007).

I23448 (Richards et al. 1987) as has CO emission (Wouterloot & Brand 1989).

4.3. On the evolutionary stages of the sources of the survey

To estimate the evolutionary stage of the sources presented in this paper, we searched the literature for the presence of dense gas, outflow and maser emission. All this information is summarized in Table 12. The table shows that there are five sources with dense gas and maser emission associated, thus possibly being the youngest regions in the survey. This is supported by the evolutionary classifications of Hill et al. (2007) and Longmore et al. (2007) for the formation of high mass stars. According to these authors, the earliest stages corresponding to a high mass "starless core" are characterized by cool (≲20 K) millimeter/dense gas emission with no maser or centimeter emission associated yet. After this stage, the first signposts of the massive protostar are traced by warm (≳50 K) millimeter emission and class I/II-methanol maser emission (Ellingsen et al. 2007), which corresponds to the "hot-core" phase, not detected in the centimeter range yet. Finally, when the YSO starts the hydrogen burning, it starts ionizing the surrounding gas and it can be detected in the centimeter range, while the YSO is still accreting part of its final mass. H₂O and OH maser emission may be present at this last stage (Ellingsen et al. 2007). Thus, as a first approach, the UCH II regions associated with millimeter continuum emission, dense gas and maser emission can be considered younger than the UCH II regions without.

In an attempt to better classify our UCH II regions in an evolutive sequence, we studied the morphology of the centimeter and millimeter emissions, and the relation between them.

From the separation between both peaks of emission, listed in Table 12, one can see that there are four UCH II regions clearly associated with a compact millimeter peak (I04579, I19045, I22198, and NGC 7538-IRS9), suggesting that the natal cloud has not yet been significantly disrupted by the massive YSO.

We quantified the degree of disruption of the natal cloud by comparing the millimeter flux density encompassed in a region very close to the centimeter peak position with the total millimeter flux density. More precisely, on one hand, the total millimeter flux density was evaluated as the flux density inside a 0.5 pc-diameter region (the typical size of massive dense cores, e.g., Beltrán et al. 2006b; Zinnecker & Yorke 2007), centered on the centimeter peak position, $S_{0.5}$. The fixed diameter of 0.5 pc allows us to exclude the contamination of the measured flux density from nearby YSO or dense clouds. On the other hand, we evaluated the millimeter flux density inside a 0.2 pc-diameter region (the size of the IRAM 30 m beam at the distance of the farthest source of this survey) centered on the position of the centimeter peak, $S_{0.2}$. We defined the *disruption degree* as

$$\text{Disruption degree} = 1 - \frac{S_{0.2}}{S_{0.5}} \,. \tag{1}$$

Thus, a low disruption degree indicates that the millimeter emission is concentrated inside a 0.2 pc-diameter region around the centimeter peak position, while a high disruption degree indicates that the millimeter emission spreads out in a 0.5 pc-diameter region. Taking into account the pointing errors of the IRAM 30 m telescope, we estimated an error of ~4% for the values of the disruption degree.

The disruption degree defined in this way should evaluate to what extent the massive YSO has pushed out and dispersed
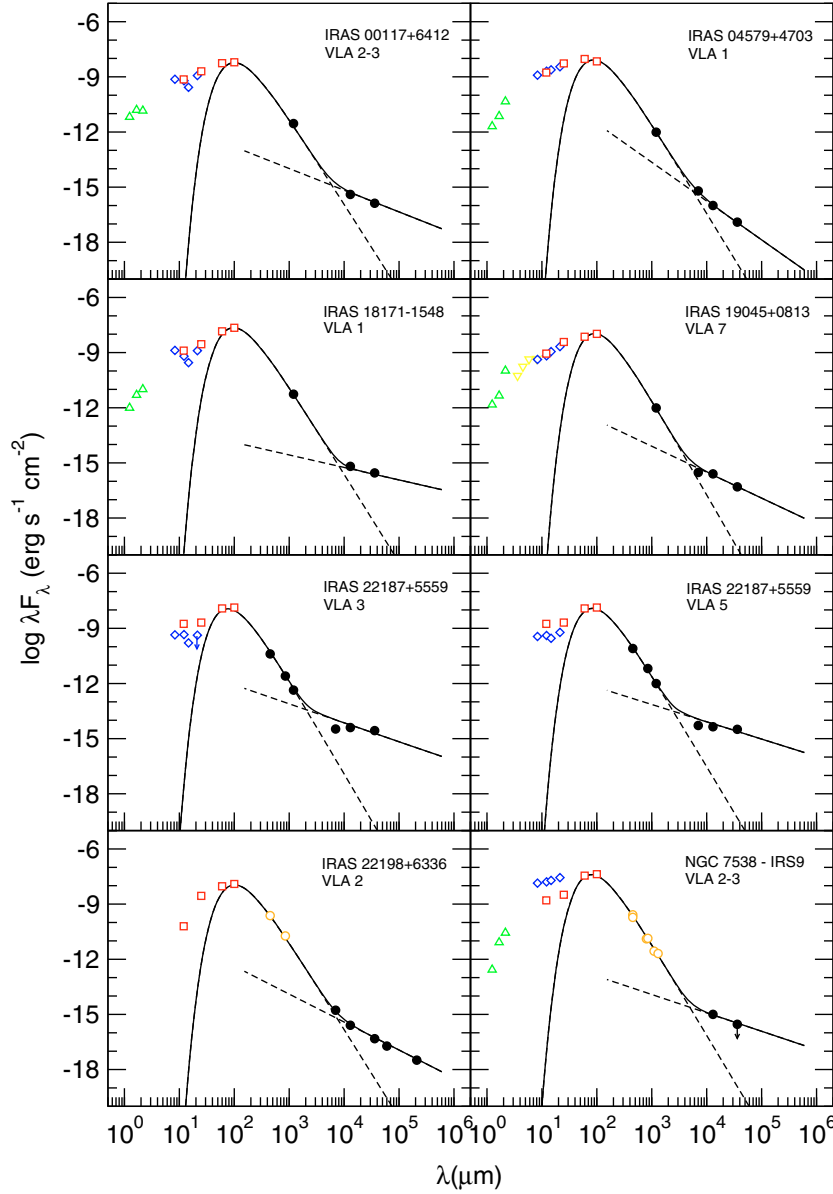
Fig. 11. Spectral Energy Distributions. Green open up-triangles: 2MASS data. Yellow open down-triangles: IRAC-*Spitzer* data. Blue open diamonds: MSX data. Red open squares: IRAS data. Orange open dots: millimeter and submillimeter data from Jenness et al. (1995) for IRAS 22198+6336, and from Sandell & Sievers (2004) for NGC 7538-IRS9. Black dots: this work, and submillimeter data from SCUBA (JCMT) for IRAS 22187+5559. Dashed lines: modified blackbody and free-free optically thin fits for the far-infrared to centimeter wavelengths. Black line: sum of the modified blackbody law and the free-free optically thin law. The results of the fit are shown in Table 11. Note that there is no attempt to fit the near- and mid-infrared wavelengths.

the natal gas and dust. In Table 12 the regions are ordered from smallest to largest disruption degree, listed in Col. (6). From the table, one can see that the sources with smallest disruption degrees, <70%, are I22198, I19045, I04579, and NGC 7538-IRS9. If the cloud is disrupted by the expansion of the UCH II region then one would expect to find a correlation between the size of the centimeter source and the disruption degree. Such a correlation is clear in Fig. 12, where we plot the disruption degree versus the size of the centimeter source.

The disruption degree and the centimeter size could be affected not only by the expansion of the H II region (an evolutionary effect), but also by the initial density of the natal cloud. For example, de Pree et al. (1995) find that for initial higher densities of the natal cloud the sizes of the UCH II regions associated are smaller. Similarly, the disruption degree could be affected by

the initial density of the cloud: the smaller the initial density, the larger the disruption degree. In addition, inhomogenities in the medium surrounding the massive YSO could produce an accumulation of matter where the density is higher, shifting the peak of millimeter emission from the centimeter peak, as could be the case of I22187 (see Sect. 4.2.7). However, several arguments are against the interpretation of the disruption degree as tracing only the initial conditions. First, in the first stages of the formation of a massive YSO (assuming no close companions), the YSO has to be associated with millimeter flux at least as strong as its surroundings (e.g., Hill et al. 2007). Second, we found small values of the disruption degree for the regions that we previously classified as less evolved judging from dense gas and maser emission (see above). In addition, we note that our sample does not show an important correlation between the size of the centimeter
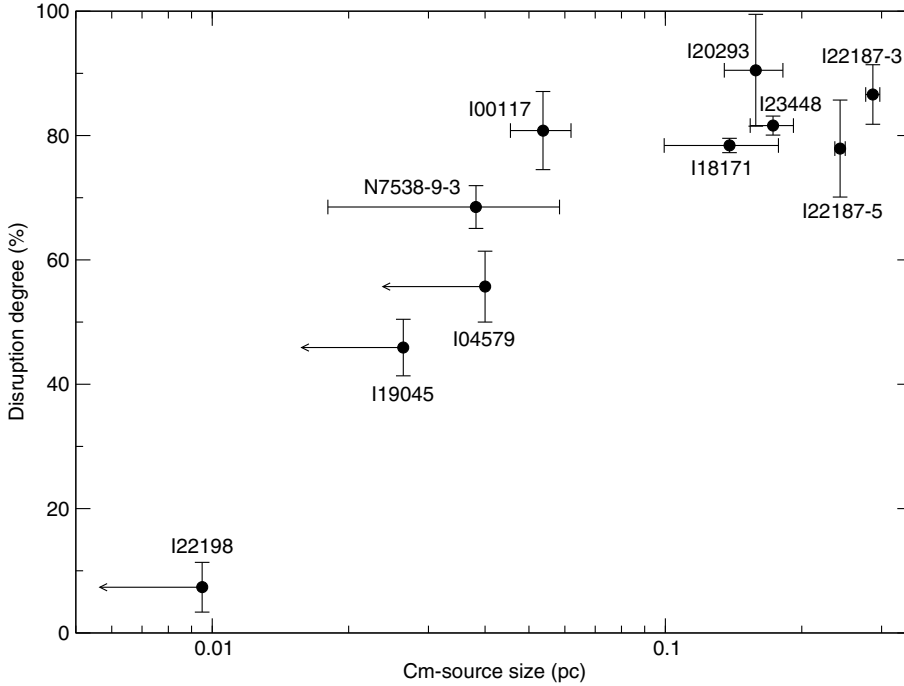
Fig. 12. Disruption degree of the natal cloud defined as one minus the ratio of the millimeter flux density picked up within a ~0.2 pc-diameter region (the size of the IRAM 30 m beam at the distance of the farthest source of this survey) centered on the centimeter peak position and the millimeter flux density picked up within a ~0.5 pc-diameter region (the typical size of massive dense cores) also centered on the centimeter peak position, versus the size of the centimeter source (from Table 10). For the disruption degree the errors have been estimated taking into account the pointing errors of the IRAM 30 m telescope. For the cm-size we estimated the error from the Gaussian fit obtained with the task JMFIT in AIPS.

source and the bolometric luminosity. So, the disruption degree seems to be more related to the evolution of the massive YSO than to the initial properties of the cloud.

Even more relevant is that our classification from the disruption degree is consistent with the infrared properties and in particular with the infrared excess derived from the 2MASS data, which should also be indicative of the evolutionary stage (Sect. 3.3). We found that the source with the smallest disruption degree in our survey, I22198, has no near- (2MASS source) or mid-infrared (MSX source) emission, suggesting that this YSO is deeply embedded in gas and dust, which is opaque to the infrared emission. Regions with (slightly) larger disruption degree are I19045, I04579, and NGC 7538-IRS9, the three showing red or orange infrared excess (Sect. 3.3). For these sources the centimeter emission is compact and spatially coincident with the millimeter emission, which is compact as well. Sources with larger disruption degrees such as I18171 and I00117, for which the millimeter emission appears clumpy, extended, and/or displaced from the centimeter peak, have smaller infrared excesses (yellow). Finally, sources with the largest disruption degrees (I23448, I20293) have a centimeter emission that is less compact, with the millimeter emission dispersed around the centimeter source, and the infrared excess being among the smallest in the sample. Thus, our sample contains intermediate/high mass star-forming regions that can be ordered in an evolutionary sequence, from regions containing massive YSOs deeply embedded in the natal cloud to regions with massive YSOs whose ionizing photons are in the process of completely disrupting the natal cloud.

5. Conclusions

We observed, with the IRAM 30 m telescope and the VLA, the continuum emission at 1.2 mm, 1.3 cm and 3.6 cm toward a sample of 11 intermediate/high mass star-forming regions not previously observed at millimeter and/or centimeter wavelengths. Nine were observed in the millimeter range and 10 in the centimeter range (8 coinciding with the regions observed at IRAM 30 m). Additionally, four of the most promising regions

were observed with the VLA at 7 mm. Our main conclusions can be summarized as follows:

1. From the IRAM 30 m observations we found 1.2 mm emission in all regions but I18212. Four regions have very extended and weak emission, while the other six show a clear emission peak with some substructure. We derived the mass of gas and dust traced at 1.2 mm, finding values from 10 to 140 $M_\odot$.
2. From the centimeter VLA observations we found 3.6 cm emission in all regions, most of it from compact sources. At 1.3 cm, all regions but I18123 have emission associated with some 3.6 cm sources and a centimeter source is found within or near the IRAS error ellipse. We estimated the spectral indices of the central sources (those lying within the central 50″ around the IRAS source) to be between 3.6 and 1.3 cm. Additionaly, we searched the NVSS for emission at 21 cm, and estimated the spectral index between 21 and 3.6 cm. For most of the sources associated with the IRAS source we found flat or positive spectral indices, suggesting that the emission comes from compact or UC H II regions, thermal radiojets or externally ionized globules. Deconvolved sizes of the centimeter sources range from <0.01 to 0.3 pc, and the physical parameters of the H II regions indicate that the ionizing stars are early B-type stars.
3. For the four regions observed at 7 mm the emission was partially resolved. Taking into account the spectral index between 3.6 and 1.3 cm, we were able to derive the dust contribution to the 7 mm continuum emission for I04579 and I22198, which is around 40% for both sources.
4. By combining our data with the infrared surveys of 2MASS, MSX, and IRAS, and with IRAC-*Spitzer* data (when available), we built the SED and fitted a modified blackbody law taking into account the contribution of a free-free optically thin law for the centimeter observations. We found median values of ~25 $M_\odot$ for the mass, ~29 K for the dust temperature, and ~1.9 for the dust emissivity index of the envelope of each intermediate/high mass YSO.

5. By studying the morphology of the centimeter and millimeter emission, and the separation between both peaks of emission, we found a correlation between the degree of disruption of the natal cloud (estimated from the millimeter flux detected within a ~0.2 pc-diameter region, centered at the position of the centimeter peak, and the millimeter flux within a ~0.5 pc-diameter region), and the size of the centimeter source. This allowed us to establish an evolutionary sequence for the UCH II regions studied in this work, which is consistent with the expected evolutionary stage from the dense gas, outflow, and maser emission, as well as with the infrared properties of the sources associated with the UCH II regions. Thus, we classified our sources from the youngest, I22198, similar to the Class 0 low mass sources, with no near- or mid-infrared emission, to the most evolved, I23448 and I20293, with the centimeter source(s) having disrupted the molecular natal cloud.

References

Allen, L. E., Calvet, N., D'Alessio, P., et al. 2004, ApJS, 154, 363
Anglada, G. 1995, Rev. Mex. Astron. Astrof. Conf. Ser., 1, 67
Bachiller, R., Gomez-Gonzalez, J., Barcia, A., & Menten, K. M. 1990, A&A, 240, 116
Beltrán, M. T., Estalella, R., Anglada, G., Rodríguez, L. F., & Torrelles, J. M. 2001, AJ, 121, 1556
Beltrán, M. T., Cesaroni, R., Codella, C., et al. 2006a, Nature, 443, 427
Beltrán, M. T., Brand, J., Cesaroni, R., et al. 2006b, A&A, 447, 221
Bernasconi, P. A., & Maeder, A. 1996, A&A, 307, 829
Beuther, H., Schilke, P., Sridharan, T. K., et al. 2002, A&A, 383, 892
Boogert, A. C. A., Blake, G. A., & Tielens, A. G. G. M. 2002, ApJ, 577, 271
Brand, J., Cesaroni, R., Caselli, P., et al. 1994, A&AS, 103, 541
Briggs, D. 1995, Ph.D. Thesis, New Mexico Inst. of Mining and Technology
Bronfman, L., Nyman, L.-A., & May, J. 1996, A&AS, 115, 81
Carilli, C. L., & Holdaway, M. A. 1997, Millimeter Array Technical Memo, 173 (NRAO)
Carral, P., Kurtz, S. E., Rodriguez, L. F., de Pree, C., & Hofner, P. 1997, ApJ, 486, L103
Casoli, F., Combes, F., Dupraz, C., Gerin, M., & Boulanger, F. 1986, A&A, 169, 281
Cesaroni, R., Palagi, F., Felli, M., et al. 1988, A&AS, 76, 445
Cesaroni, R., Felli, M., Testi, L., Walmsley, C. M., & Olmi, L. 1997, A&A, 325, 725
Cesaroni, R., Felli, M., Jenness, T., et al. 1999, A&A, 345, 949
Condon, J. J., Cotton, W. D., Greisen, E. W., et al. 1998, AJ, 115, 1693
Curiel, S., Canto, J., & Rodriguez, L. F. 1987, Rev. Mex. Astron. Astrofis., 14, 14, 595
Davis, C. J., Moriarty-Schieven, G., Eislöffel, J., Hoare, M. G., & Ray, T. P. 1998, AJ, 115, 1118
Edris, K. A., Fuller, G. A., & Cohen, R. J. 2007, A&A, 465, 865
Ellingsen, S. P., Voronkov, M. A., Cragg, D. M., et al. 2007 [arXiv:0705.2906]
Di Francesco, J., Johnstone, D., Kirk, H., MacKenzie, T., & Ledwosinska, E. 2008 [arXiv:0801.2595]
Felli, M., Brand, J., Cesaroni, R., et al. 2007, A&A, 476, 373
Furuya, R. S., Kitamura, Y., Wootten, A., Claussen, M. J., & Kawabe, R. 2003, ApJS, 144, 71
Galt, J. A., Kwok, S., & Frankow, J. 1989, AJ, 98, 2182
Garay, G., Brooks, K. J., Mardones, D., & Norris, R. P. 2006, ApJ, 651, 914
Garay, G., Mardones, D., Brooks, K. J., Videla, L., & Contreras, Y. 2007, ApJ, 666, 309
Getman, K. V., Feigelson, E. D., Garmire, G., Broos, P., & Wang, J. 2007, ApJ, 654, 316
Gibb, A. G., & Hoare, M. G. 2007, MNRAS, 380, 246
Gibb, A. G., Hoare, M. G., Little, L. T., & Wright, M. C. H. 2003, MNRAS, 339, 1011
Gómez, Y., Rodríguez, L. F., Girart, J. M., Garay, G., & Martí, J. 2003, ApJ, 597, 414
de Gregorio-Monsalvo, I., Gómez, J. F., Suárez, O., et al. 2006, ApJ, 642, 319
Hartmann, L., Megeath, S. T., Allen, L., et al. 2005, ApJ, 629, 881
Hasegawa, T. I., & Mitchell, G. F. 1995, ApJ, 441, 665
Hill, T., Burton, M. G., Cunningham, M. R., & Minier, V. 2007 [arXiv:0705.4623]
Hillenbrand, L. A. 1995, Ph.D. Thesis, University of Massachusetts
Hillenbrand, L. A., & Hartmann, L. W. 1998, ApJ, 492, 540
Ignace, R., & Churchwell, E. 2004, ApJ, 610, 351
Jenness, T., Scott, P. F., & Padman, R. 1995, MNRAS, 276, 1024
Kameya, O., Morita, K.-I., Kawabe, R., & Ishiguro, M. 1990, ApJ, 355, 562
Kenyon, S. J., & Hartmann, L. 1995, ApJS, 101, 117
Keto, E., Zhang, Q., & Kurtz, S. 2008, ApJ, 672, 423
Kim, K.-T., & Kurtz, S. E. 2006, ApJ, 643, 978
Kumar, M. S. N., & Grave, J. M. C. 2007, A&A, 472, 155
Kumar, M. S. N., Keto, E., & Clerkin, E. 2006, A&A, 449, 1033
Kurtz, S. 2005, Massive Star Birth: A Crossroads of Astrophysics, IAUS, 227, 111
Larionov, G. M., Val'tts, I. E., Winnberg, A., et al. 1999, A&AS, 139, 257
Lefloch, B., Lazareff, B., & Castets, A. 1997, A&A, 324, 249
Longmore, S. N., Burton, M. G., Barnes, P. J., et al. 2007, MNRAS, 379, 535
Massi, F., Giannini, T., Lorenzetti, D., et al. 1999, A&AS, 136, 471
Matsuyanagi, I., Itoh, Y., Sugitani, K., et al. 2006, PASJ, 58, L29
Mitchell, G. F., & Hasegawa, T. I. 1991, ApJ, 371, L33
Molinari, S., Brand, J., Cesaroni, R., & Palla, F. 1996, A&A, 308, 573
Mookerjea, B., Sandell, G., Stutzki, J., & Wouterloot, J. G. A. 2007, A&A, 473, 485
Mueller, K. E., Shirley, Y. L., Evans, N. J., II, & Jacobson, H. R. 2002, ApJS, 143, 469
Nguyen-Q-Rieu, Epchtein, N., Truong-Bach, & Cohen, M. 1987, A&A, 180, 117
Nürnberger, D. E. A. 2003, A&A, 404, 255
Ossenkopf, V., & Henning, T. 1994, A&A, 291, 943
Palla, F., Brand, J., Comoretto, G., Felli, M., & Cesaroni, R. 1991, A&A, 246, 249
Panagia, N. 1973, AJ, 78, 929
Patel, N. A., Curiel, S., Sridharan, T. K., et al. 2005, Nature, 437, 109
de Pree, C. G., Rodriguez, L. F., & Goss, W. M. 1995, Rev. Mex. Astron. Astrofis., 31, 39
Reed, B. C. 2003, AJ, 125, 2531
Reid, M. A., & Wilson, C. D. 2005, ApJ, 625, 891
Richards, P. J., Little, L. T., Heaton, B. D., & Toriseva, M. 1987, MNRAS, 228, 43
Rieke, G. H., & Lebofsky, M. J. 1985, ApJ, 288, 618
Sandell, G., & Sievers, A. 2004, ApJ, 600, 269
Sandell, G., Goss, W. M., & Wright, M. 2005, ApJ, 621, 839
Slysh, V. I., Dzura, A. M., Val'tts, I. E., & Gerard, E. 1994, A&AS, 106, 87
Sridharan, T. K., Beuther, H., Schilke, P., Menten, K. M., & Wyrowski, F. 2002, ApJ, 566, 931
Strom, K. M., Strom, S. E., & Merrill, K. M. 1993, ApJ, 412, 233
Tafalla, M., Bachiller, R., & Martin-Pintado, J. 1993, ApJ, 403, 175
Tamura, M., Gatley, I., Joyce, R. R., et al. 1991, ApJ, 378, 611
van der Tak, F. F. S., & Menten, K. M. 2005, A&A, 437, 947
Testi, L., Palla, F., & Natta, A. 1998, A&AS, 133, 81
Testi, L., Palla, F., & Natta, A. 1999, A&A, 342, 515
Testi, L., Palla, F., & Natta, A. 2000, Stellar Clusters and Associations: Convection, Rotation, and Dynamos, 198, 211
Tofani, G., Felli, M., Taylor, G. B., & Hunter, T. R. 1995, A&AS, 112, 299
Valdettaro, R., Palla, F., Brand, J., et al. 2002, A&A, 383, 244
van der Walt, D. J., Gaylard, M. J., & MacLeod, G. C. 1995, A&AS, 110, 81
Wilking, B. A., Blackwell, J. H., Mundy, L. G., & Howe, J. E. 1989, ApJ, 345, 257
Wouterloot, J. G. A., & Brand, J. 1989, A&AS, 80, 149
Wouterloot, J. G. A., Brand, J., & Fiegle, K. 1993, A&AS, 98, 589
Zapata, L. A., Rodríguez, L. F., Kurtz, S. E., O'Dell, C. R., & Ho, P. T. P. 2004, ApJ, 610, L121
Zapata, L. A., Palau, A., Ho, P. T. P., et al. 2008, A&A, 479, L25
Zhang, Q., Hunter, T. R., Brand, J., et al. 2005, ApJ, 625, 864
Zheng, X.-W., Zhang, Q., Ho, P. T. P., & Pratap, P. 2001, ApJ, 550, 301
Zinnecker, H., & Yorke, H. W. 2007, ARA&A, 45, 481